HiSST: International Conference on
High-Speed Vehicle Science Technology

26–29 November 2018, Moscow, Russia

Analysis of Hypersonic Model Pitching Experiments in the TUSQ Facility.

Nathan Stern[1], Ingo Jahn[2], Rishabh Choudhury[3,4], Fabian Zander[5], Johan Steelant[6], and David R. Buttsworth[7]

Abstract

Experiments have been performed in the TUSQ hypersonic facility on the control of hypersonic models using 3D printed test models fitted with on-board actuation and data-sampling electronics. Analysis of experiments on a pivoted body with an actuated elevator is proceeding through the use of analytical and computational simulations. Our aim is to quantify the impact of the boundary layer separation in the body-elevator corner region on the dynamics of the pitching model, and to attempt to emulate the control loop and responses in the dynamic simulations, to match the physical results. Static pressures measured at three locations along the body and elevator, and pitching moment measurements are assessed against simulations from shock-expansion theory applied to the measured, instantaneous body and elevator angles. A similar assessment of the experiments is performed using 3D CFD simulations of static combinations of body and elevator angles, and additional 2D simulations of the dynamically-actuated aerodynamic model are also performed.

Keywords: *Hypersonics, Computational Fluid Dynamics (CFD), TUSQ*

1. Introduction

The USQ hypersonic wind tunnel facility (TUSQ) provides Mach 5.85 flow durations of 200 ms, making it suitable for ground-test development of hypersonic control strategies. Experiments with models containing actuation and pressure sampling electronics have already been performed with the objective of demonstrating a practical platform from which hypersonic control methods can be physically tested [2, 11]. It is expected that data-sets generated in this manner can also be utilised to verify CFD results for both static conditions, and dynamically-actuated simulations. One of our aims is to identify the significance of unsteady boundary-layer separation effects associated with the pitching model with elevator actuation. This paper presents the results in three parts; initially an overview of the physical model and components will be presented, followed by 3D steady-state CFD analysis of the model and elevator at discrete angles using the DLR TAU-Code. Finally the current dynamic control CFD simulations performed using Eilmer 4 are presented.

[1]*Postgraduate Student, School of Mechanical and Electrical Engineering, University of Southern Queensland. nathan.stern@usq.edu.au*

[2]*Senior Lecturer, School of Mechanical and Mining Engineering, The University of Queensland. i.jahn@uq.edu.au*

[3]*Vice-Chancellor's Research Fellow, School of Mechanical and Electrical Engineering, University of Southern Queensland. rishabh.choudhury@usq.edu.au*

[4]*International Research Fellow, ESA-ESTEC, Aerothermodynamics and Propulsion Analysis Section TEC-MPA, Noordwijk, The Netherlands, rishabh.choudhury@esa.int*

[5]*Lecturer, School of Mechanical and Electrical Engineering, University of Southern Queensland. fabian.zander@usq.edu.au*

[6]*Senior Research Engineer, Aerothermodynamics and Propulsion Analysis Section TEC-MPA, Noordwijk, The Netherlands. johan.steelant@esa.int.*

[7]*Professor, School of Mechanical and Electrical Engineering, University of Southern Queensland. david.buttsworth@usq.edu.au*

2. Physical Model

A complete overview of the components used in the physical model is given in [11]. What follows here is an overview, and a discussion of issues found during physical testing.

2.1. Component Overview

The physical test model consists of a 10 mm thick and 55 mm wide 3D printed flat plate with a sharpened leading edge (10° half-angle), freely pivoted near the front of the model, as shown in Figure 1. The rear 15 mm of the model was a hinged and actuated control surface. Three pressure sensors (Amphenol NPP-301-100A absolute pressure sensors) were positioned on the upper surface of the model and elevator.

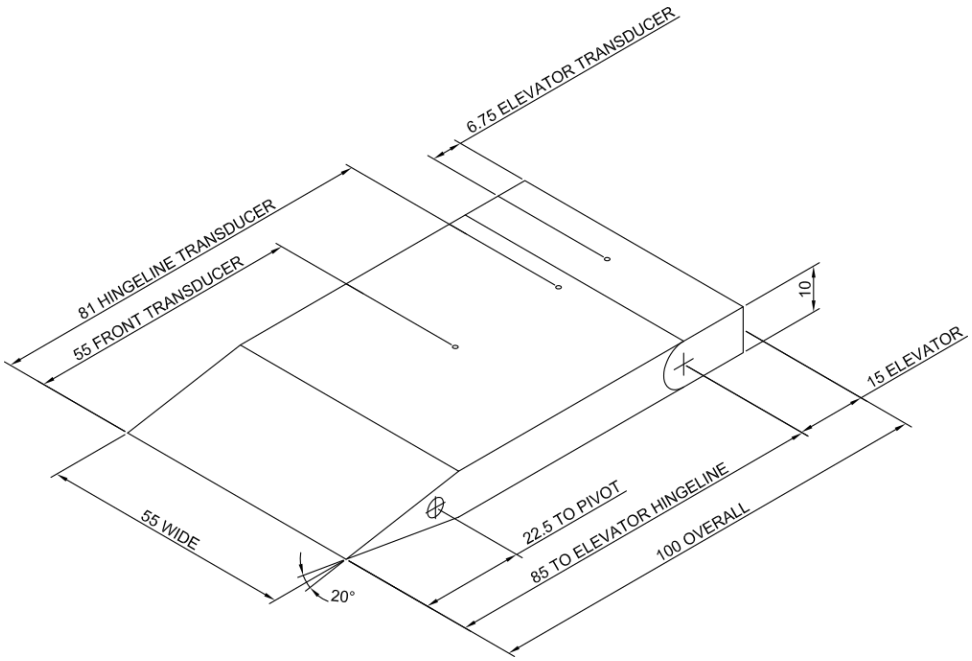

Figure 1. Model geometry and transducer locations.

The model included an elevator which was actuated by on-board electronics, using a small DC motor and hall effect sensor to provide elevator position feedback to a PID loop controller. All three pressure transducers are located along the model center-line. The front transducer is located to sample pressures independent of the elevator deflection effects. The hinge-line transducer is positioned to sample pressures associated with boundary layer and compression corner effects immediately upstream of the elevator. The elevator transducer is located at 55% of the elevator chord. Pressures sampled by this transducer are treated as a reference for the entire control actuation surface. Figure 2 shows the components used and final assembly.

Each of the three Amphenol NPP-301-100A 100 kPa pressure transducers was connected to its own analogue-front-end (AFE) pre-amplifier. The AFE pre-amplifiers each consisted of an Analog Devices AD8321 digitally-tuneable gain instrumentation amplifier, and Linear Technologies LTC1523, 100 kHz 4th order low-pass Butterworth filter. The gain was set in software for all AFE channels to 320. The main system is controlled using an STMicroelectronics SM32F407VGT micro-controller (MCU), with pressure data logged to a microSD card. An Invensense MPU6000 Inertial Measurement Unit (IMU) was used to record the body pitch angles. A Pololu sub-micro motor with integral 136:1 gearbox was used for elevator surface actuation, with the elevator position being detected using a Texas Instruments DRV5053 Analog-Bipolar Hall Effect Sensor mounted in the model body, and rare-earth magnets mounted within the elevator.

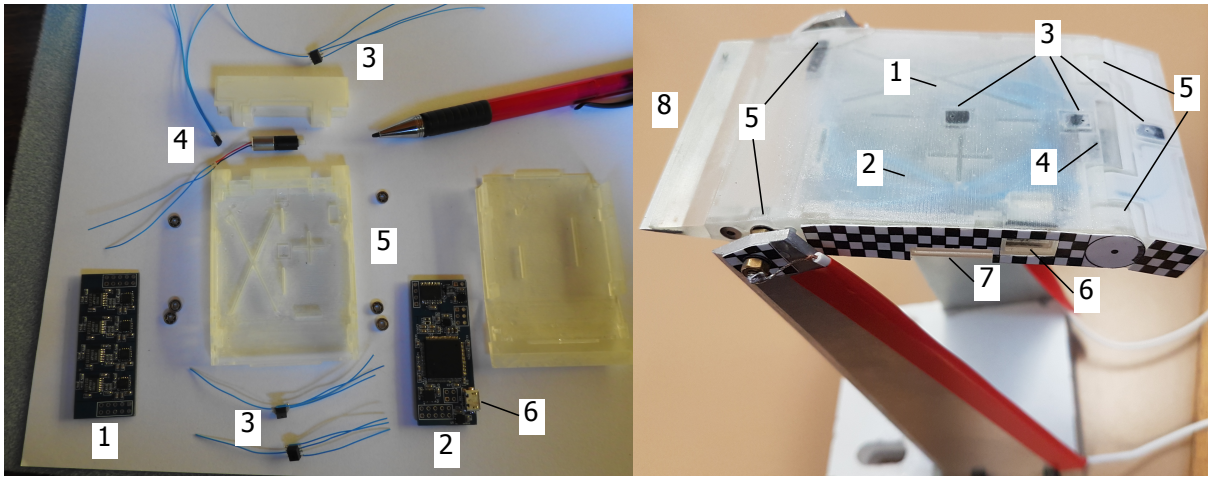

Figure 2. Image of the model during and after assembly. Parts are 1: AFE board. 2: MCU mainboard containing IMU, motor driver and data-logger. 3: Pressure transducers. 4: motor and position sensor. 5: 2 mm ball bearings. 6: Comm port. 7: SD card slot. 8: Sharpened aluminium alloy leading edge.

2.2. Experimental Results - Motion Analysis

A simple 'bang-bang' control approach was used for the initial control experiments. The on-board IMU was sampled at 8 kHz, providing rotational rate data in the pitch axis. The sign of this rate signal was used to generate a position command for the elevator. The MCU compared the elevator's actual position with this position command, with the difference between the two being treated as a position error. This position error was then applied to a closed loop PID controller, with the output of this controller being used to generate the DC motor drive signal. The gearbox on the motor exhibited approximately 6° of backlash. This backlash adversely affected the controllability of the model as discussed in [11]. The PID controller architecture was adapted from [13].

A complete block diagram of this control system including the gearbox backlash is shown in Figure 3. The loop control uses elevator position to control body pitch rate. The Derivative term is computed on position feedback, rather than the error signal.

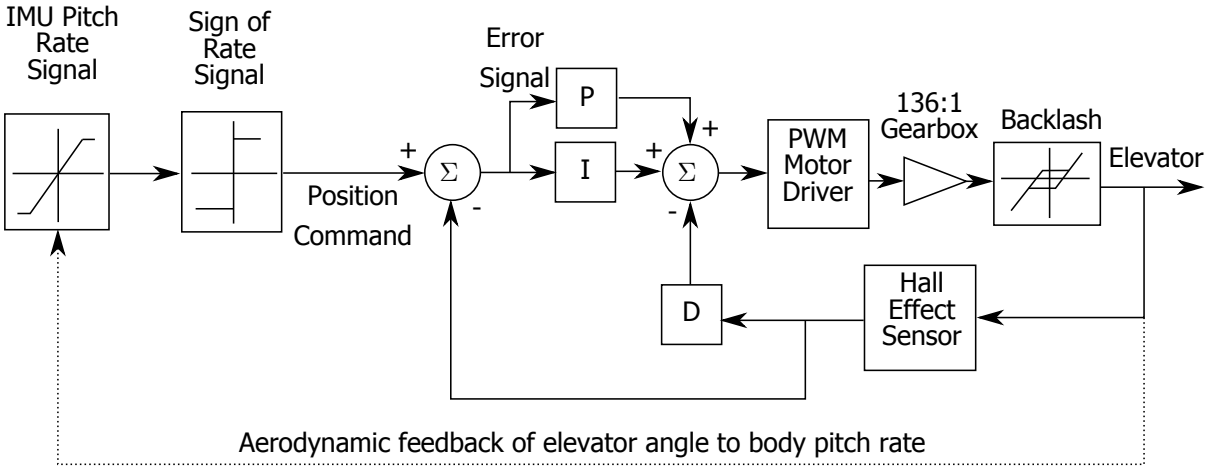

Figure 3. The complete control loop used in the experimental models. The 136:1 gearbox integral to the motor exhibited 6° of backlash.

Motion of the model as recorded by the IMU is shown in Figure 4 for three runs. In each case the body of the model was started at a nose-high/tail-low Angle of Attack (AOA) of $-10°$ with the convention being as the rear of the model moves upwards, the AOA in the plots becomes positive.

In Figure 4a, the elevator was ordered to hold 0° with respect to the body. The motion of this plot is a simple harmonic pitching as the undamped model is moved purely by the aerodynamic pressures on the model surface. The model's natural frequency with no elevator actuation is 23.26 Hz.

Figure 4b shows the first of the control experiments. Although the control loop was set to try and null out the harmonic motion of the body, the 6° of backlash in the motor contributed a 7 ms lag to the controller; at the model's own harmonic frequency, the backlash effects resulted in a total phase lag of the controller of 208°, leading to unstable control and an amplified motion.

In Figure 4c the control signal was inverted in software, giving a 180° phase shift to the controller. This initially resulted in the harmonic motion attenuating up to 100 ms into the run. However as the oscillations slowed, the phase shift again resulted in instability, this time at lower frequencies; future work will focus on dynamically calculated phase compensation techniques which are a function of the model's instantaneous pitching frequency.

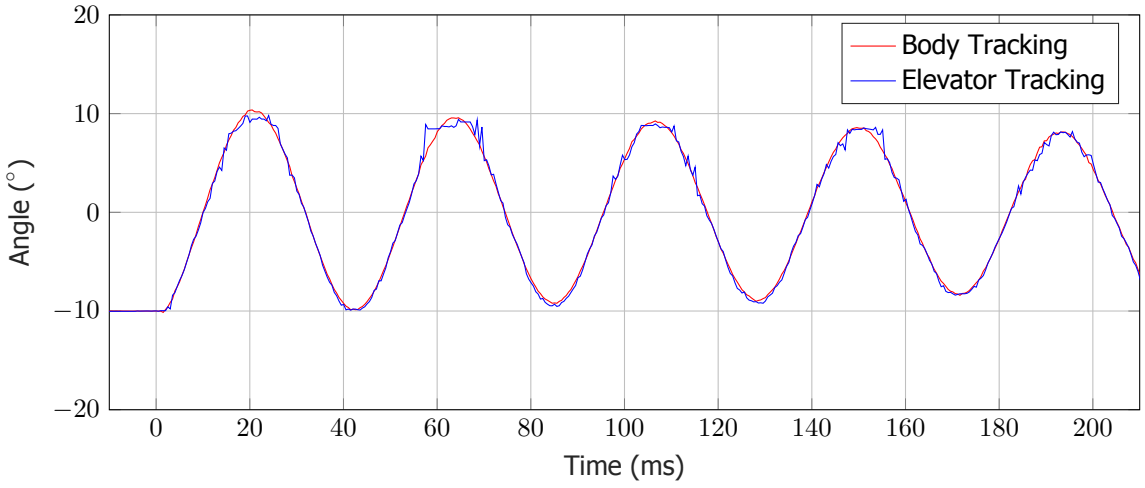

(a) No Commmand

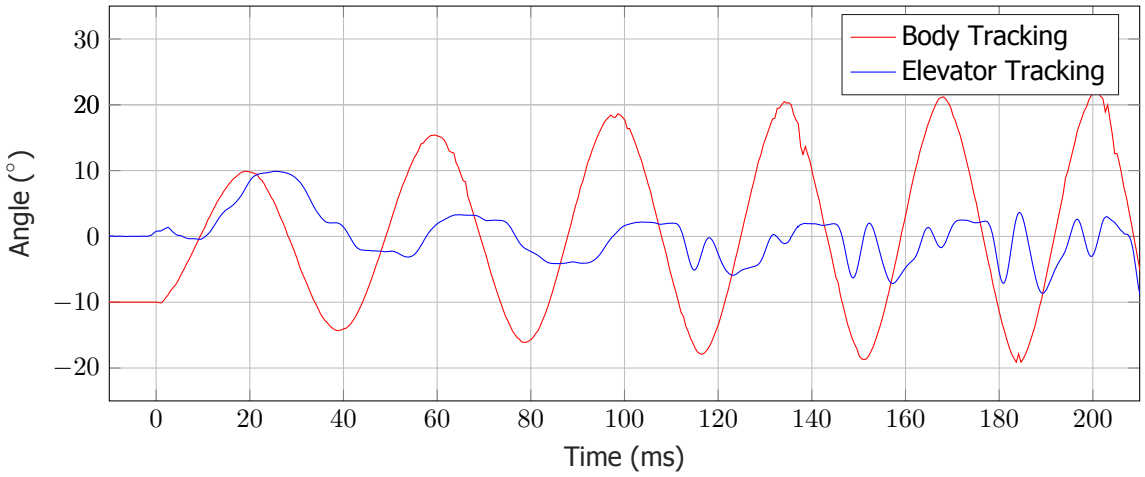

(b) Amplified Motion

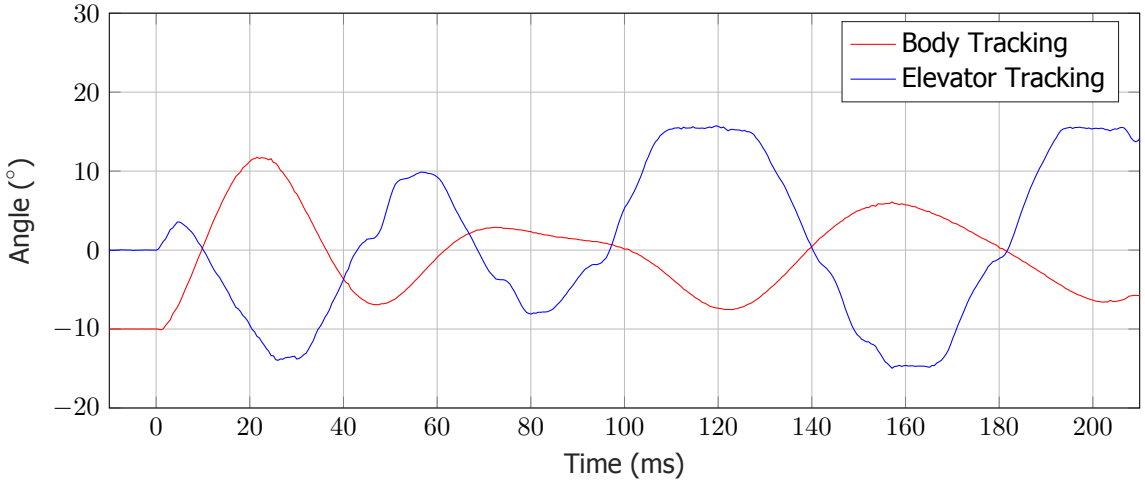

(c) Attenuated Motion

Figure 4. Body and elevator angles vs. time during hypersonic testing. Angles of body are shown relative to flow direction; angles of elevator are shown relative to body in parts (b) and (c), and relative to the flow in part (a).

2.3. Experimental Results - Pressure Analysis

Pressure was recorded throughout each experiment at three points on the model using Amphenol NPP-301 surface-mount transducers. While these sensors give a good accuracy and high bandwidth, it was discovered that the body sensor experienced clipping at lower pressures. This was ultimately attributed to the pressure transducer itself; this sensor exhibited a differential voltage 10 mV lower than the other two at a given pressure. At a gain of 320, this subsequent 3.2 V DC offset exceeded the range of DC reference adjustment available on the AFE board. This caused the amplifier to clip at pressures below 750 Pa. The results of the pressure measurements during the run are shown in Figure 6, with sub-figures 6a to 6c corresponding to the body and elevator motions respectively in sub-figures 4a to 4c.

The NPP-301 transducers are a typical Wheatstone bridge construction, with the exception of having two ground connections to the sensor itself: the 'left' and 'right' halves of the bridge are isolated from each-other inside the sensor, permitting calibration and adjustment of the transducers themselves prior to use by addition of balancing resistors between the sensor and battery ground. For the current experiments no resistor was fitted; both halves were simply tied to ground as per a standard Wheatstone bridge transducer configuration.

The manufacturer's specification for the NPP-301 transducers states an offset tolerance of $\pm 10\,\mathrm{mV\,V^{-1}}$. To avoid clipping in future experiments, individual sensors will be calibrated and any offsets compensated for prior to mounting in the model; sensors are placed in the high-vacuum test section at TUSQ and evacuated down to <1 Pa. The resistances through the bridge halves are measured, then the ground wires are connected and the sensor energised. The differential voltage is then recorded. This process is repeated as the vacuum chamber is vented up to atmospheric pressure.

Figure 5 shows the results of four new NPP-301 transducers, intended for future experiments. Sensors 2 to 4 will be included in the next model, as they show the closest uncompensated differential voltages.

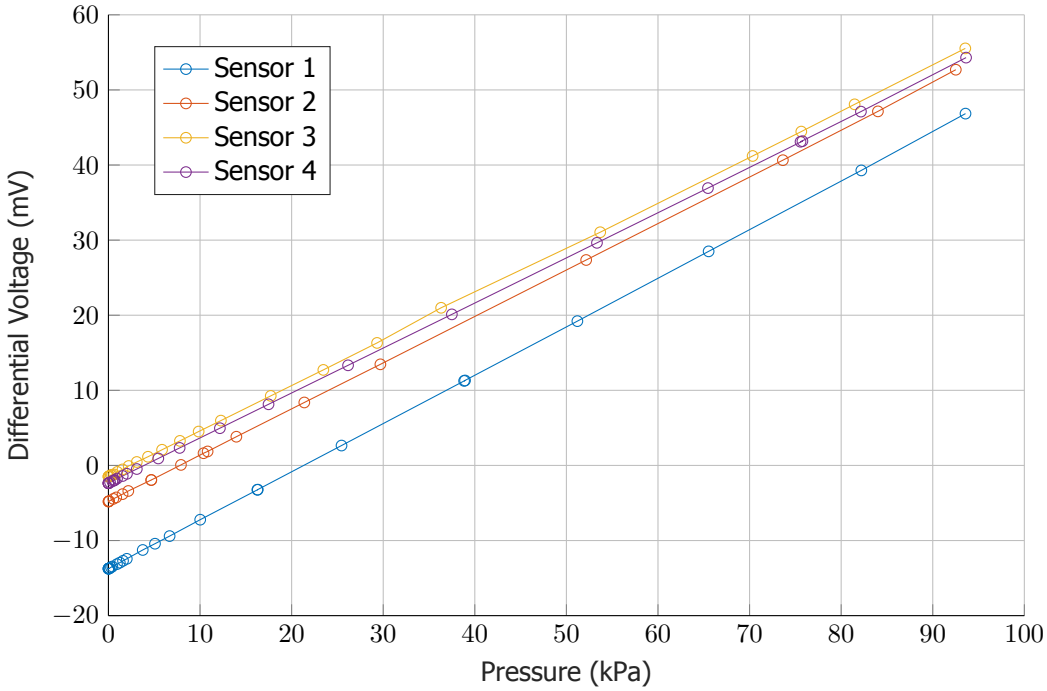

Figure 5. Results of calibrating four randomly chosen NPP-301 pressure transducers, of a batch intended for future experiments.

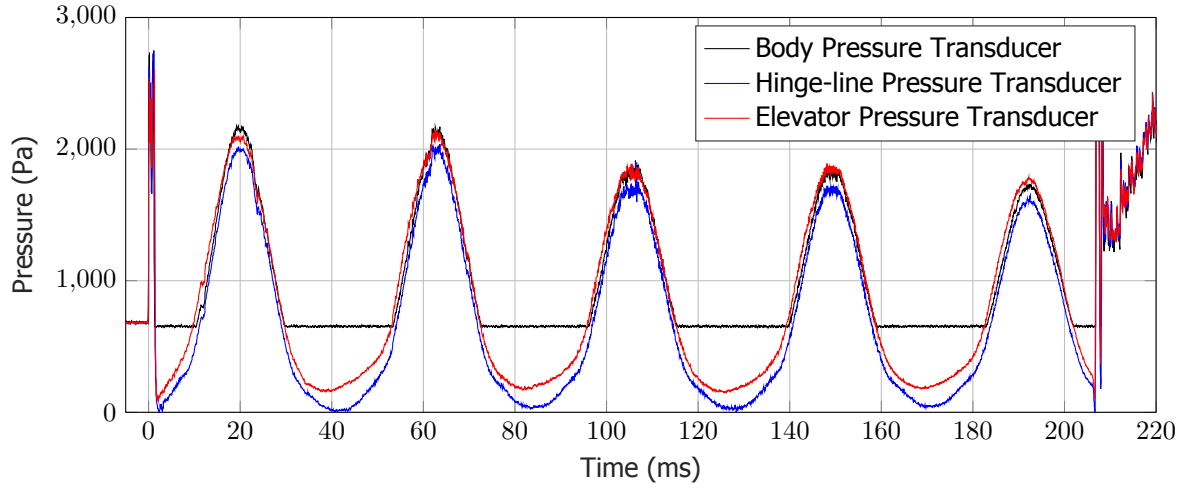

(a) Pressure results of the no-command run, as seen in Figure 4a.

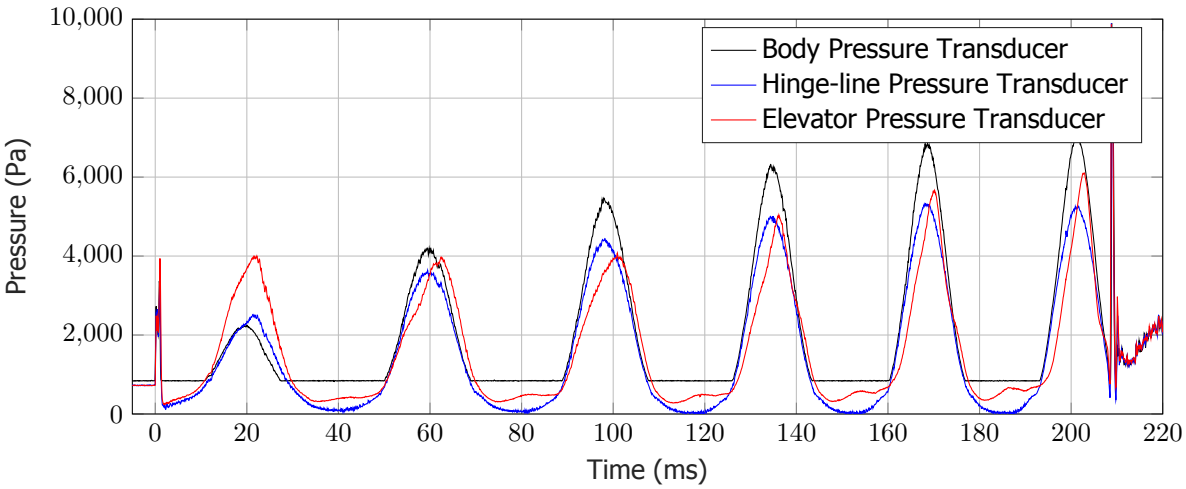

(b) Pressure results of the amplified motion run, as seen in Figure 4b.

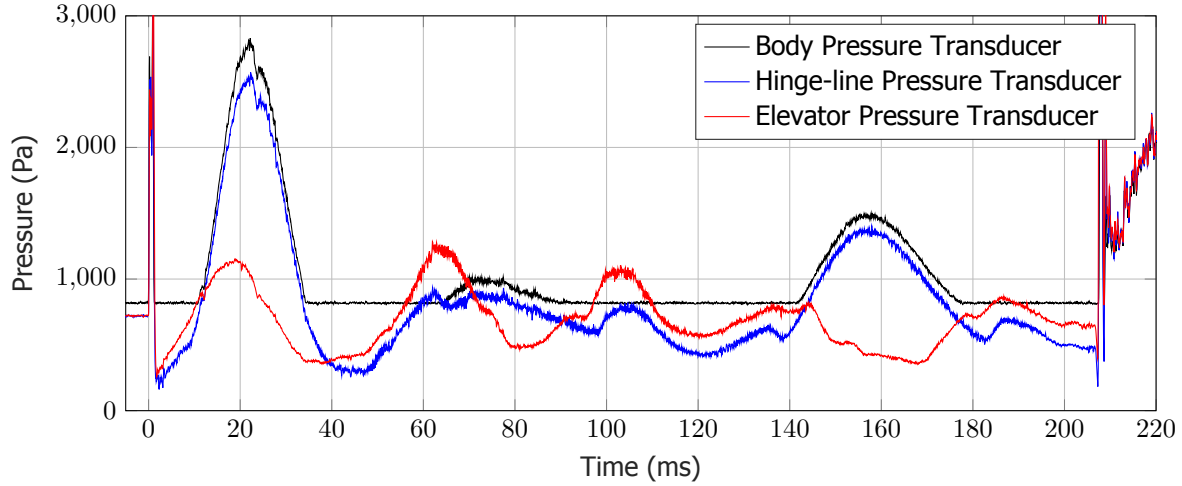

(c) Pressure results of the attenuated motion run, as seen in Figure 4c.

Figure 6. Plots of pressures across the surface of the model for each of the respective runs shown in Figure 4.

2.4. Experimental Results - Mathematical analysis using Shock Expansion Theory

A first attempt to mathematically simulate the pressures measured in the preceding section is presented here, using Shock Expansion theory.

Oblique Shockwave The model nose facet has a 10° half angle, as shown in Figure 2. At Angles of Attack above $-10°$ The upper nose facet is behind an oblique shock, while the body facet is behind an expansion fan. The elevator can also generate a compression effect which can be modelled as a shock wave for positive deflection angles. The same relationships exist on the underside facets at Angles of Attack below 10° and negative elevator angles. From [6], the equation for oblique shockwaves is given in equation 1, and solved numerically for β.

$$tan(\delta) = \frac{2cot\beta(M_1^2 sin^2\beta - 1)}{2 + M_1^2(\gamma + cos(2\beta))}\,, \tag{1}$$

where:

- δ is the turning angle due to the model facet. In the case of the nose facet, this is AOA + 10°, relative to the flow direction.
- β is the shock wave angle, in degrees.

Pressure behind the oblique shock is:

$$P_2 = P_1\left(1 + \frac{2\gamma}{\gamma+1}(M_1^2 sin^2\beta - 1)\right), \tag{2}$$

where subscripts 1,2 indicate respectively, upstream and downstream of the shock.

To compute the subsequent downstream flow, the Mach number behind the oblique shock is required, given as:

$$M_2 = \frac{1}{sin(\beta - \delta)}\sqrt{\frac{1 + \frac{\gamma-1}{2}M_1^2 sin^2\beta}{\gamma M_1^2 sin^2\beta - \frac{\gamma-1}{2}}}\,. \tag{3}$$

Prandtl-Meyer expansion fan The change in model geometry between the leading edge and body facets causes a Prandtl-Meyer expansion fan. The change in flow angle between the body and elevator can also produce an expansion fan effect; on the upper surface at negative elevator angles and on the underside at positive deflection angles. The equation for which is:

$$\nu_0 = \sqrt{\frac{\gamma+1}{\gamma-1}}\cdot tan^{-1}\sqrt{\frac{\gamma-1}{\gamma+1}(M_0^2 - 1)} - tan^{-1}\sqrt{M_0^2 - 1}\,. \tag{4}$$

In the case of the change of facet angle between the nose and body facets on the model is 10°, and this is added as a constant:

$$\nu_1 = \nu_0 + 10^\circ\,. \tag{5}$$

The Mach number behind the fan is then solved implicitly as:

$$\nu_1 = \sqrt{\frac{\gamma+1}{\gamma-1}}\cdot tan^{-1}\sqrt{\frac{\gamma-1}{\gamma+1}(M_1^2 - 1)} - tan^{-1}\sqrt{M_1^2 - 1}\,. \tag{6}$$

Variables for equations 4 - 6 are:

- ν_0, ν_1 are the isentropic changes in angle of the flow direction.
- M_0, M_1 are respectively the Mach numbers upstream and downstream of the expansion fan.

At AOA $< -10°$ the upper nose facet of the model goes from being behind an oblique shock to an expansion fan. Similarly, at AOA $>10°$ the underside nose facet transitions from being behind an oblique shock to an expansion fan. In these cases, the pressures over the leeward side of the body facet can be computed by taking the total turning angle. Equation 6 becomes:

$$\nu_1 = \nu_0 + AOA\,, \tag{7}$$

with M_0 taken as the free-stream Mach number.

Applying equations 1 to 5 for oblique shock and expansion fans at $M_\infty = 5.85$ gives both the downstream Mach number, and pressure ratio P/P_∞ with respect to AOA. Figure 7 gives the downstream Mach number and pressure ratio for the body facet, with respect to a changing AOA. At angles greater than $-10°$ AOA, the top of the nose facet is behind an oblique shock, while the body facet is behind a Prandtl-Meyer expansion fan. At angles below this, both the body and nose facets are behind Prandtl-Meyer expansion fans.

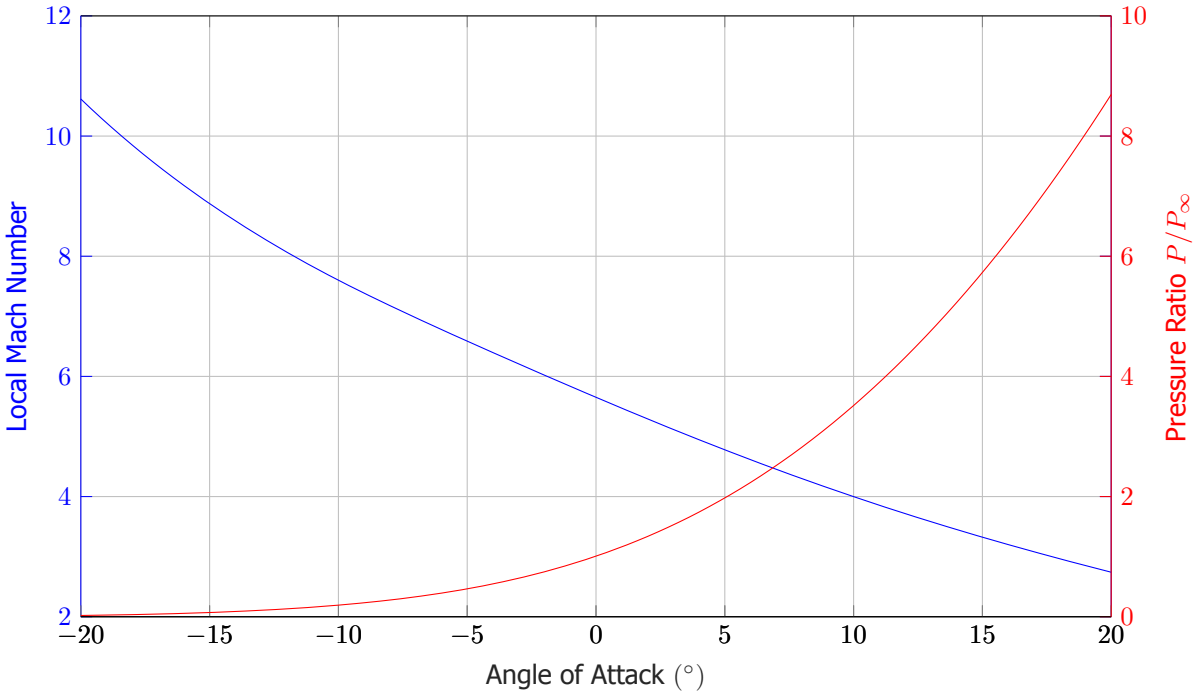

Figure 7. Mathematically computed Mach and Pressure Ratio over the body facet of the model

As discussed in [1] the free-stream Mach number for the TUSQ facility is $M_\infty = 5.85$. Temporal free-stream pressure conditions for TUSQ are shown in Figure 8, and are characterised by reflected expansion waves in the barrel. In Figure 8, the pressure measured in the barrel has been converted into a nozzle exit static pressure based on an isentropic nozzle expansion with the ratio of specific heats $\gamma = 1.4$.

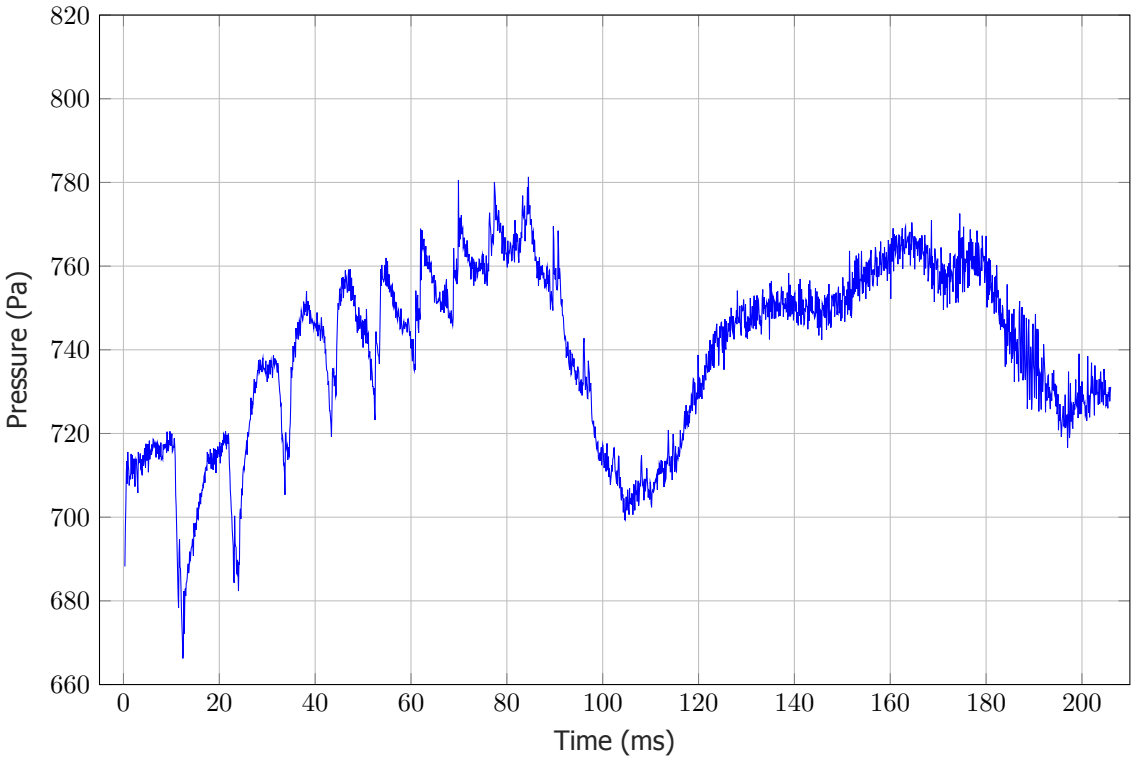

Figure 8. TUSQ Free-stream flow pressure.

Figure 9 gives the comparison between the mathematically computed pressure over the body facet in black, and the actual recorded pressures from Figure 6a in red for the front sensor (clipped data points are omitted for clarity) and blue for the hinge-line sensor. This figure was obtained by applying the body AOA motion from Figure 4a to the computed Mach and pressure ratios in Figure 7, and the temporally-varying free-stream pressures in Figure 8. It is seen that the shape of the plots matches closely at all points. However, there is a 160 Pa offset between the computed and actual values for the front sensor. This is likely due to the 3D flow effects and spillage over the sides of the model, to be discussed in the subsequent section.

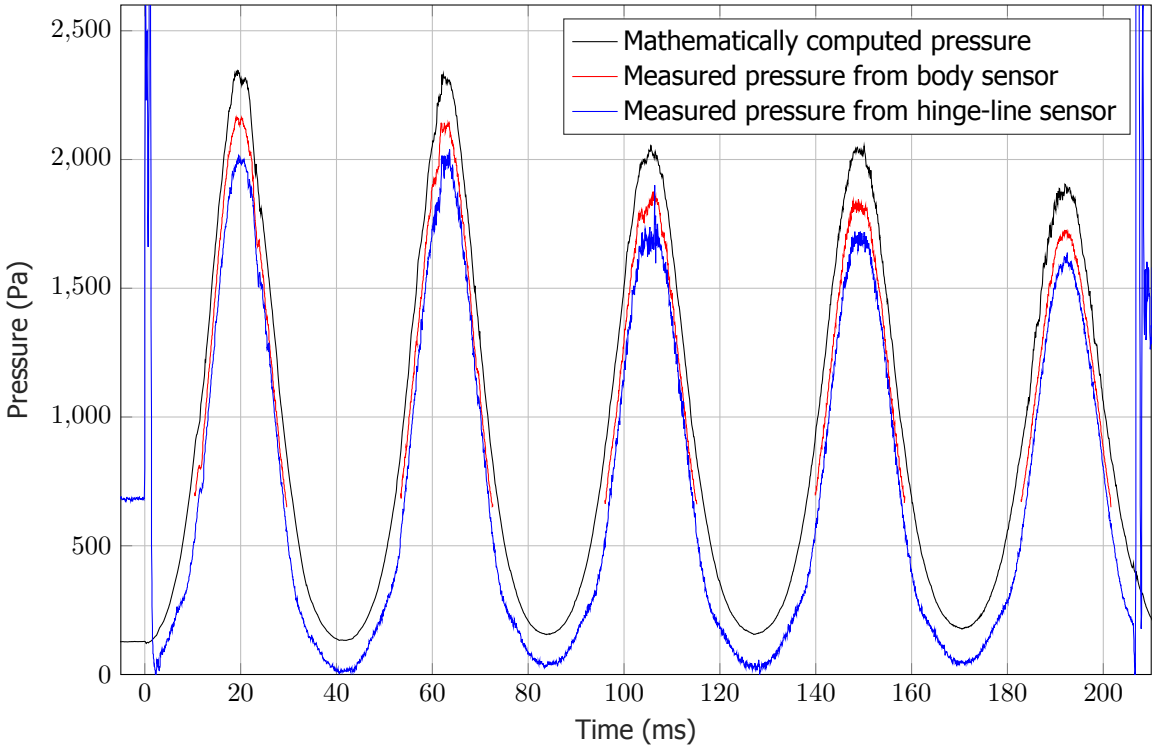

Figure 9. Mathematically computed pressures on the model upper surface, derived from body angle, using shock expansion theory. Data-points clipped by amplifier are removed for clarity.

3. CFD TAU-Code

Both 2D and 3D steady-state simulations using the DLR TAU-Code [5] were performed, with a comparison against shock expansion theory provided in this section. From these pressure plots at varying AOA and elevator angles, moments around the main body pivot were derived.

A hybrid computational grid was created for both the 2D and 3D simulations using the mesh generation software CENTAUR12.0. Several layers of prismatic elements were created at the wall surface to correctly calculate the laminar boundary layer. The first cell height normal to the wall was set to 10 µm. A structured surface grid was generated for the wing body. The total mesh count for the 3D simulations incorporating the struts was around 2.3 million nodes. The 3D mesh is shown in Figure 10.

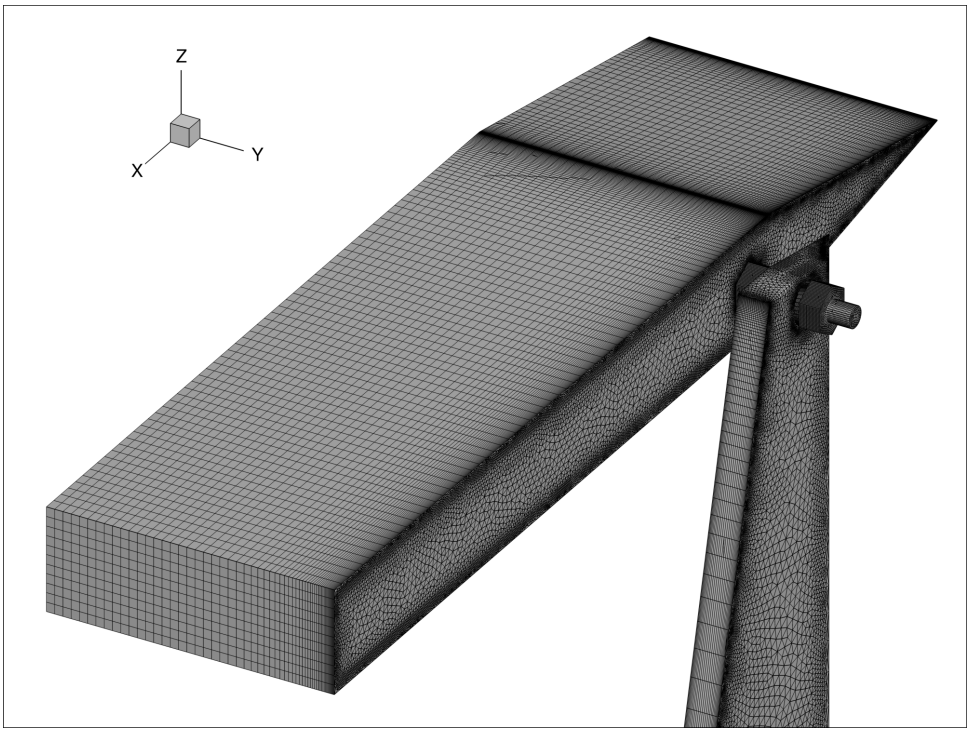

Figure 10. Surface mesh generated for the 3D wing including the strut and additional features. Model is symmetrical about the XZ plane.

The simulations were performed using the DLR TAU code [5]. The air thermal and transport properties were computed under the assumption of perfect gas, with a gas constant of 287.15 $\mathrm{J\,kg^{-1}\,K}$ and ratio of specific heat set at 1.4. A second-order upwind AUSMDV scheme by Wada and Liou [12] with a shock fix to prevent the carbuncle phenomenon was used to discretize the fluxes in the Navier-Stokes equations. A least-square reconstruction of the gradients is used, which provides more accurate results in the presence of hybrid grids. Finally, the RANS equations were integrated towards the steady solution by means of a backward Euler time-relaxation scheme. The state of the boundary layer for all the simulations was assumed to be laminar. The wall boundary condition is set to a set wall temperature of 300 K. The free-stream conditions used for the computational analysis is set at a reference Mach number of 5.85, density of 0.038 $\mathrm{kg/m^3}$ and a reference temperature of 70 K.

3.1. 2D CFD

Steady-state combinations of both elevator and Angles of Attack from $\pm 15°$ in increments of 5° were performed. Some of these 2D results are shown in Figure 11.

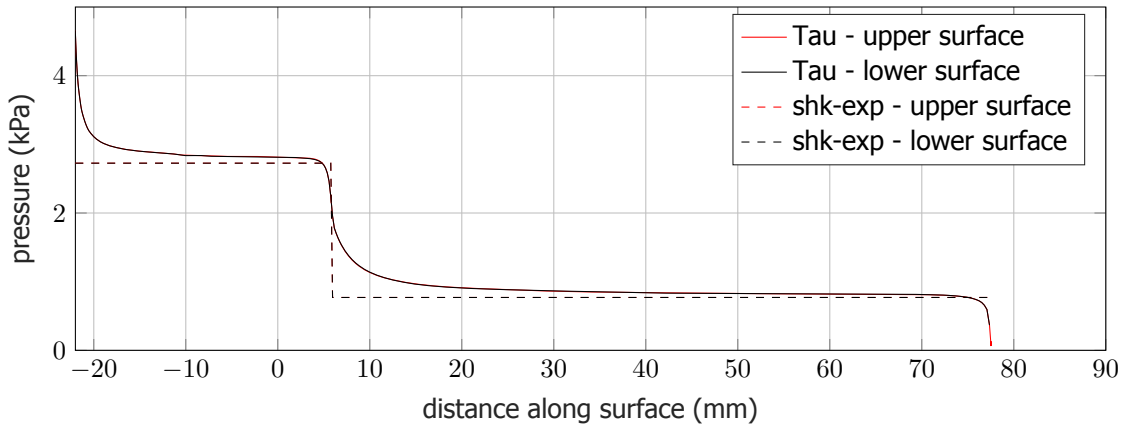

(a) Body AOA 0°, elevator 0°.

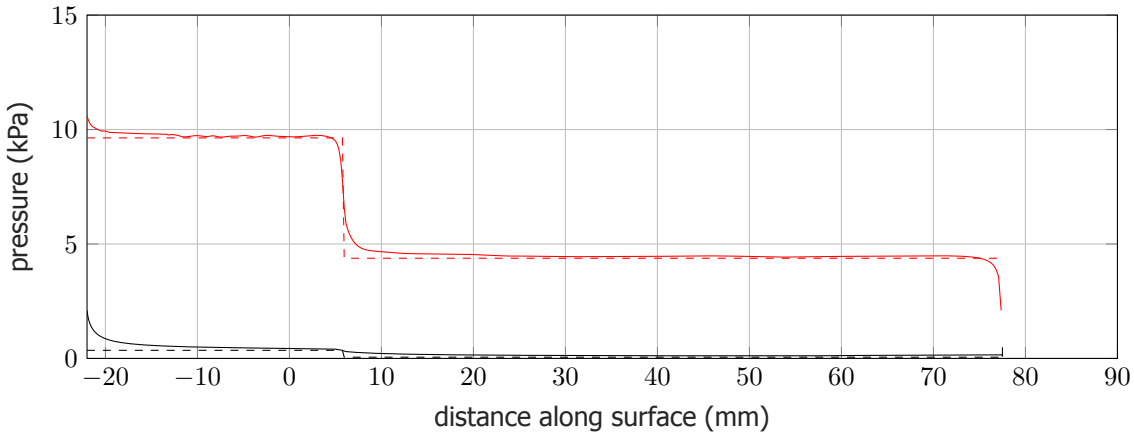

(b) Body AOA 15°, elevator 0°.

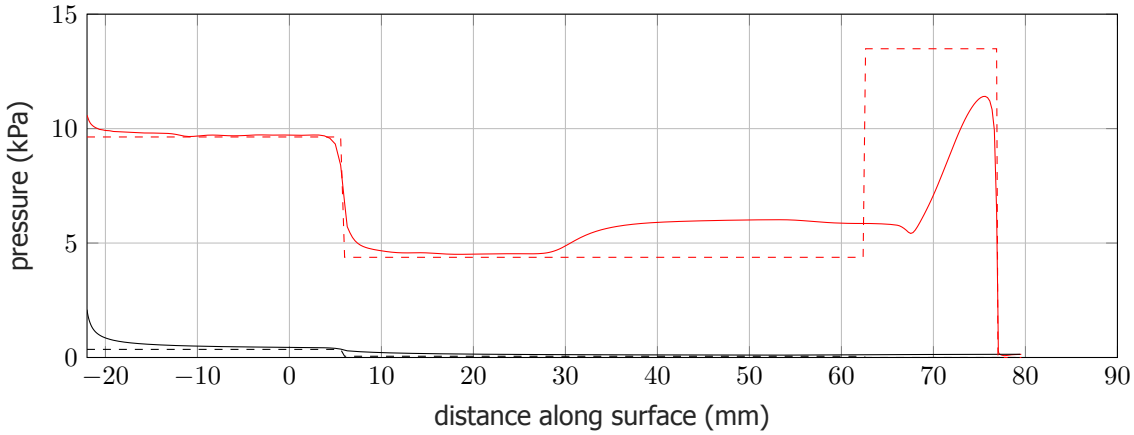

(c) Body AOA 15°, elevator 15°.

Figure 11. Comparison of TAU-Code with Shock Expansion theory for varying AOA and elevator angles.

Figure 11 shows a good correlation between shock expansion theory and the TAU-Code for the nose and

body facets. However at higher angles of elevator deflection the simulations show a separated shock forming upstream of the elevator hinge-line, as shown in Figure 11c where this shock separation begins 30 mm behind the model pivot.

2D surface pressures were assumed to be constant across the 55 mm wide model. The sum of the moments for each AOA and elevator angle are shown in Figure 12, which illustrates that the shock-expansion theory gives a good agreement with TAU at lower elevator angles. At higher elevator angles, boundary layer separation effects observed in the TAU simulations cause a rise in pressure on the body ahead of the hinge-line, and a reduction over the elevator, relative to the inviscid shock-expansion theory. An effective flow deflection occurs over the body as a result of the boundary layer separation, and thus the effective flow turning angle experienced at the elevator is reduced, and so reduces the control authority of the elevator. The shock-expansion theory therefore over-estimates the total moments on the complete model relative to the TAU simulations.

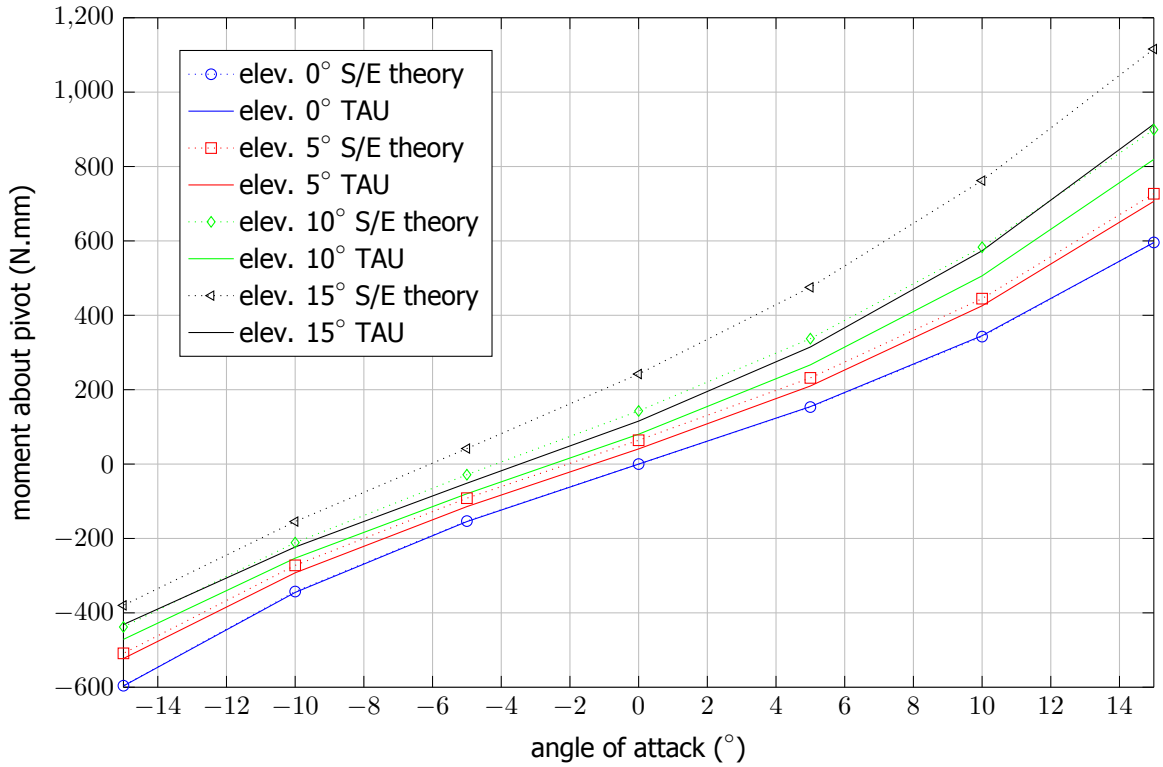

Figure 12. Comparison of moments around main pivot, between TAU and shock expansion theory.

Figure 13 shows a comparison between Schlieren photography of the physical experiment during the run, and the 2D results from TAU. AOA is 10° while the elevator is 10° in both cases. The similarity of the results is visible, particularly the shocks generated by the nose facet, and flow separation ahead of the elevator.

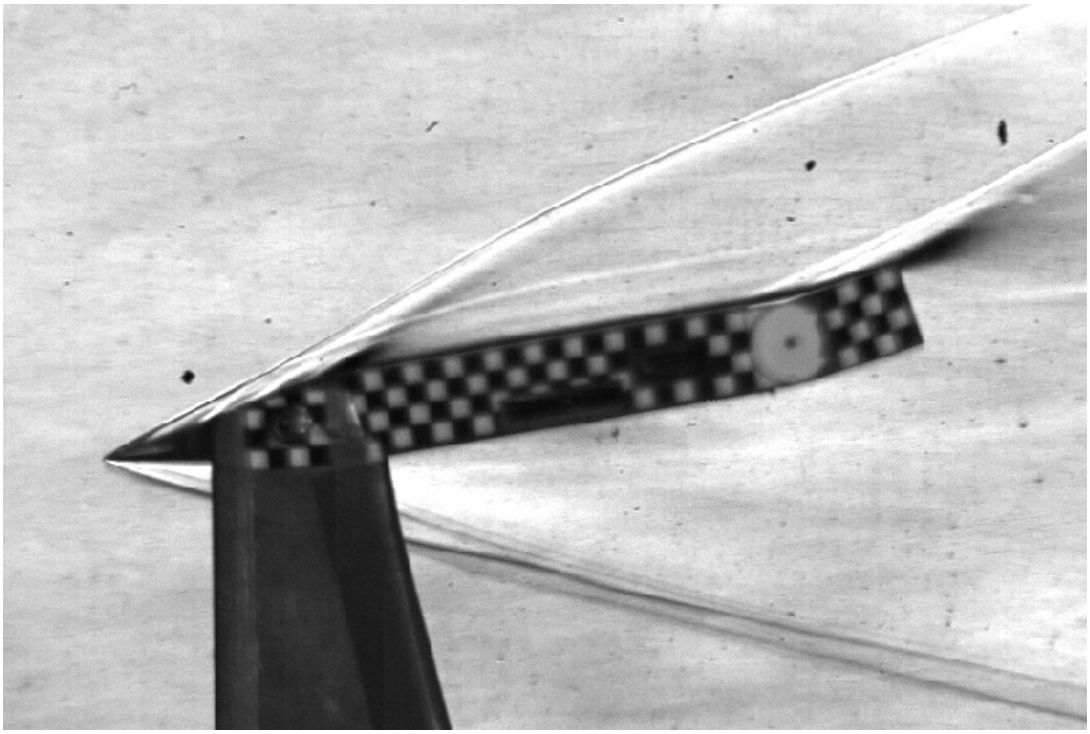

(a) Schlieren imaging of the hypersonic test model.

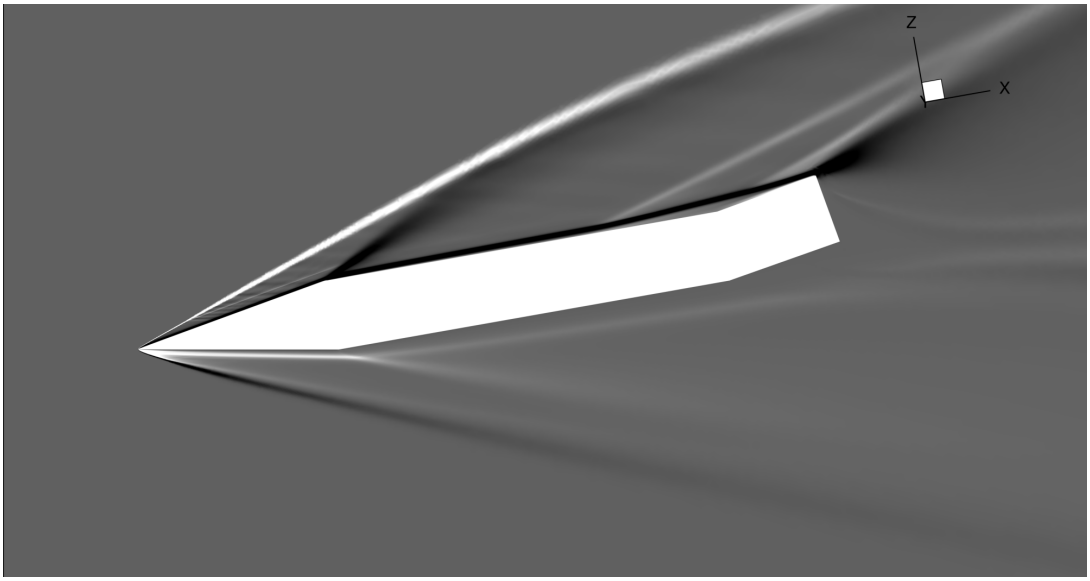

(b) DLR TAU-Code.

Figure 13. Comparison of experimental schlieren results with TAU-Code. AOA is 10°, elevator 10° in both cases.

3.2. 3D CFD

3D steady-state simulations were also performed, both treating the wing as an isolated entity, and with the inclusion of the struts which support the model pivots. 3D surface plots of the model with the colour-coded pressures overlaid are shown in Figure 14, with a plane of symmetry about the XZ-plane. From these results it can be seen that the pressure distribution in a span-wise direction is non-uniform; spillage and edge effects are visible in Figures 16a and 14c, while the addition of the strut in Figures 16b and 14d reveal that particularly at larger angles of attack, the strut generates a separated shock upstream of the pivot which spills over onto the nose facet, and also contributes to a shock impingement on the upper and lower surfaces behind the pivot.

Cross-sectional pressure distributions from Figures 14c and 14d for the AOA −10°, elevator 10° cases are shown in Figure 15, with span-wise pressure sections through the body, hinge-line and elevator pressure transducer locations shown respectively in Figures 15a, 15b and 15c. Comparisons of simulations with and without the strut show a marked difference towards the edge of the model, however along the center-line, the simulated values for both strut and no-strut cases are in good agreement. Furthermore, these simulated pressures are in reasonable agreement with the experimental data from the pressure transducers for approximately AOA −10°, elevator 10°, a configuration that occurred for the experiment illustrated in Figure 6c at the time of 20 ms.

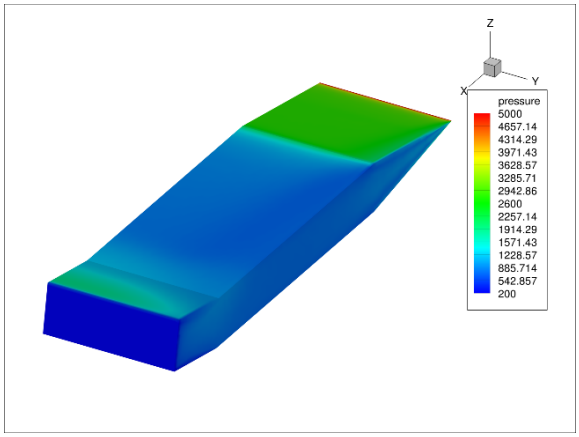

(a) No Strut, AOA 0° elevator 10°.

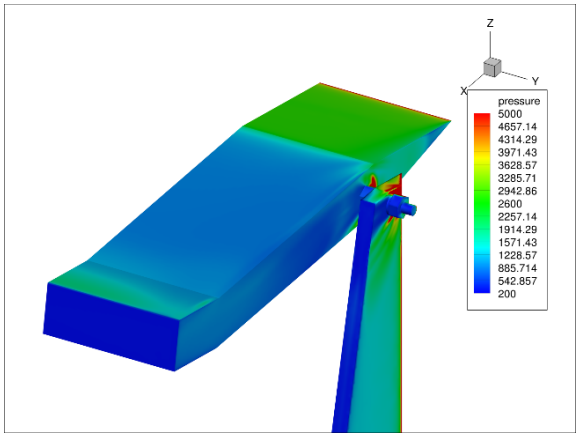

(b) Strut, AOA 0° elevator 10°.

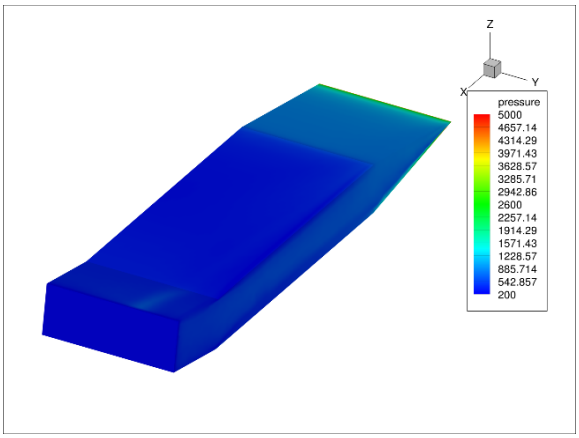

(c) No Strut, AOA −10° elevator 10°.

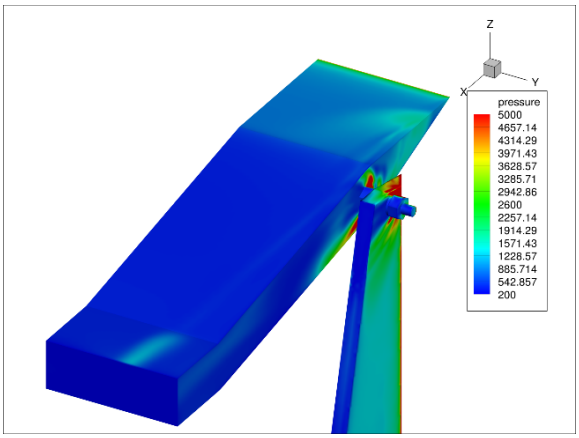

(d) Strut, AOA −10° elevator 10°.

Figure 14. TAU-Code 3D pressure distributions on the top of the model, with an XZ-plane of symmetry.

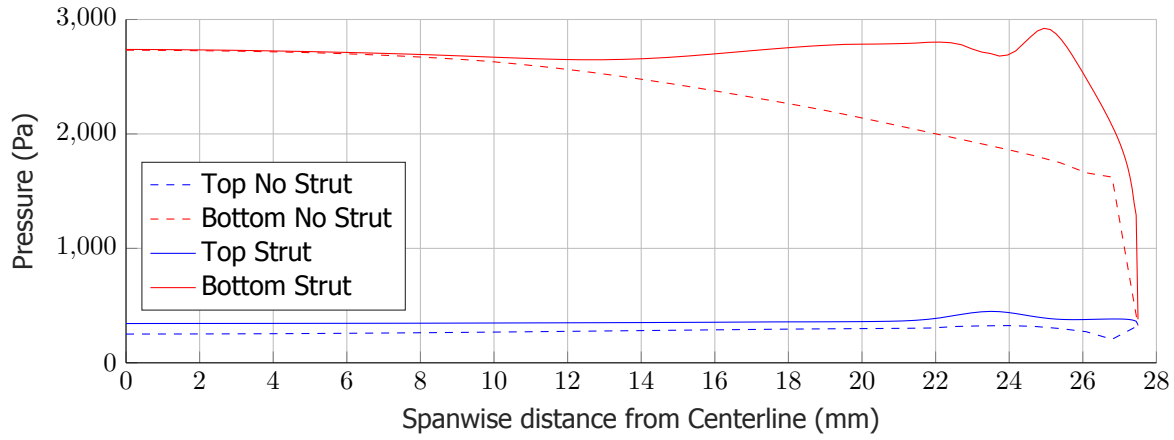

(a) Body Pressure Location.

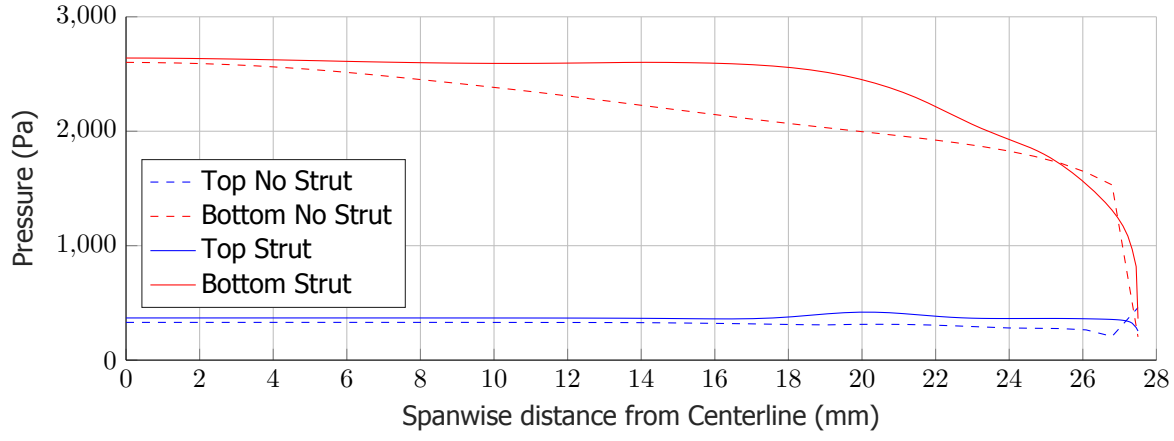

(b) Hinge-line Pressure Location.

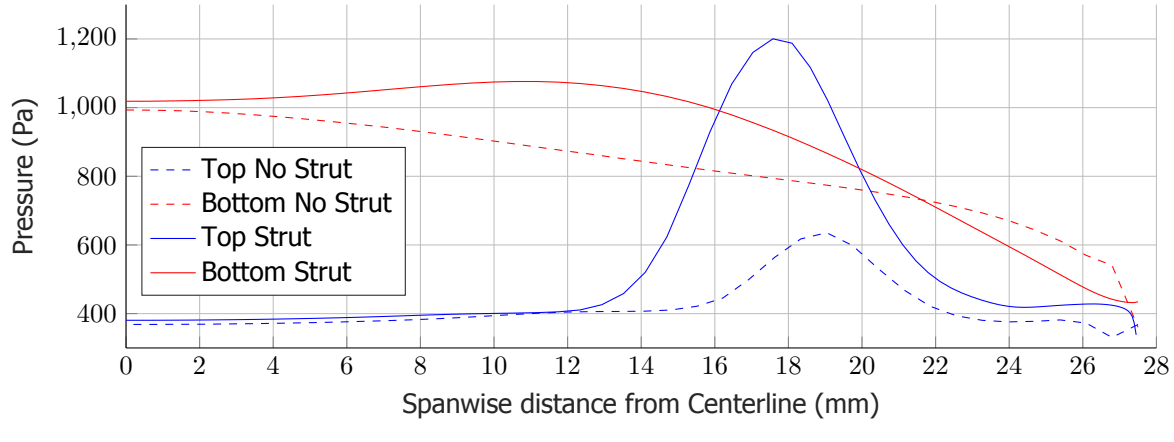

(c) Elevator Pressure Location.

Figure 15. Span-wise 3D pressure comparisons between strut and no-strut simulation, at AOA −10 degree, elevator 10 degree.

The increases in pressure on the lee-side of the model, as seen particularly in Figure 15c, 18 mm from the model center-line are salient, and can attributed to flow spillage effects: the high pressure on the windward surface causes a flow spillage towards the low pressure region on the lee-side of the model. The path of the flow from the leading edge to the trailing edge on the lee-side of the model is partially blocked by flow spillage effects at locations approaching the model edges, and thus a local region of high pressure is generated as the lee-side flow seeks to negotiate a path around such blockage effects. The flow blockage effect is amplified over the elevator when it is deflected, due to the additional compression of the flow over the elevator. Figure 16 shows Mach number contour slices through the flow-field above the surface of the model; significant flow structure is observed in both cases, but the complexity is amplified by the presence of the strut.

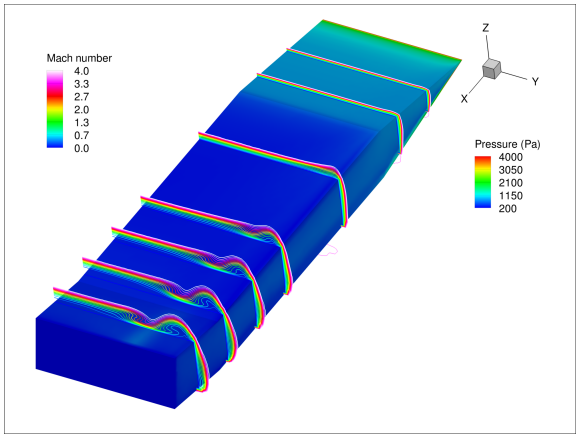

(a) No Strut, AOA −10° elevator 10°.

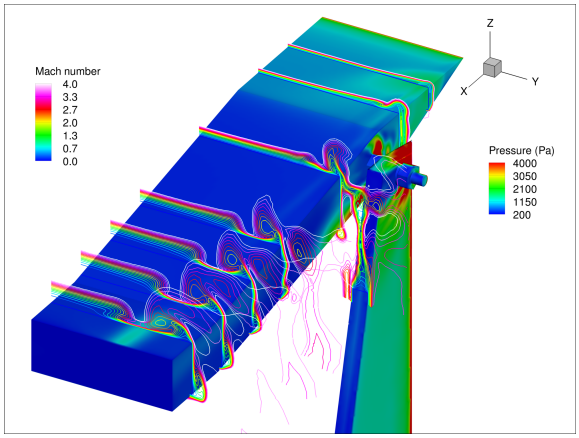

(b) Strut, AOA −10° elevator 10°.

Figure 16. Flow field non-uniformities associated with model edge effects on the leeward side of the model

Moments computed from the pressure distributions are shown in Table 1, with the 2D values from Figure 12 included for comparison.

Table 1. Comparison of sum of the moments about the pivot.

	∑ moments (N mm): 2D model only	∑ moments (N mm): 3D model only	∑ moments (N mm): 3D addition of struts
AOA 0°, elevator 0°	0	0.6	2.75
AOA 0°, elevator 10°	80.28	59.78	51.52
AOA −10°, elevator 0°	345.10	95.58	124.03
AOA −10°, elevator 10°	252.95	31.93	56.43
AOA 10°, elevator 10°	506.03	227.49	233.24

The results in Table 1 show an increase in moment between the simulations for the 3D model, and the 3D model with the inclusion of the struts; this matches the results seen in Figures 14 and 15, where additional shock effects from the support strut result in increased pressures over the surface of the model. However, the most salient point of Table 1 is the variation between 2-dimensional and 3-dimensional moments; the 2D simulation over-estimates the moment by up to a factor of 4.5 relative to the 3D simulations. This can be explained as the 2D simulations assume a uniform pressure distribution in a span-wise direction across the full width of the model. In the 3D simulations however, there is flow spillage over the sides of the model, which reduces the magnitude of the restoring moment for all

combinations of AOA and elevator deflection. These spillage effects are most pronounced towards the rear of the model, i.e., the regions that have the most significant contribution to the pitching moment.

4. CFD Eilmer 4

To further improve the understanding of the dynamic system, closely coupled fluid-structure-interaction simulations were conducted with the CFD solver Eilmer [3, 4]. Due to the high computational times required for closely coupled transient simulations, only 2-D simulations, limited to the first one hundred milli-seconds of the experiment were performed. Eilmer was developed at the University of Queensland specifically for time accurate transient simulations of hypersonic flows in shock tunnels. The Eilmer solver uses the finite volume formulation and is based on the AUSMV family of flux calculators [12]. The conserved quantities are updated explicitly and the time-step is constrained to fulfil the Courant–Friedrichs–Lewy (CFL) criterion to ensure time accurate solution of the unsteady flow. Eilmer is second-order accurate in space and time. In the proximity of strong shocks, the EFM scheme [8] is used to increase numerical diffusion and to ensure stability. The solver has undergone extensive verification and validation and has been the work-horse for expansion tunnel simulations at the Centre for Hypersonics at the University of Queensland.

The first adaptation of the solver to work with grid motion was completed by Petrie-Repar [7], and this has been further developed by Qin *et al.* [9], who report details of the implementation.

4.1. Rationale

One of the greatest difficulties with interpreting the experimental data and with the development of the accurate simulations was to correctly model the motor, including the backlash component. In the physical model, during bench testing a backlash of 5.74° was observed at the gearbox output shaft, contributing to 7 ms of lag between the motor beginning to accelerate following a command, and the output of the gearbox and hence elevator responding [11]. The aim of the lower fidelity CFD simulations with Eilmer was to incorporate a state-space-machine consisting of motor, gearbox, backlash, and elevator, so that intermediary parameters not directly measured from the experiment can be elucidated.

The system uses a torque transfer approach, whereby the torque on the elevator is treated as a product of aerodynamic forces, the elevator's own inertia, and the torque supplied by the motor and gearbox once the gears are in mesh. The core motor speed and position are computed, and then divided by a factor of 136 to give the gearbox ratio. Subsequent to this the backlash term is applied. This backlash gap, denoted by $\theta_b = 5.74°$ sets the drive condition; when the gearbox output shaft has moved more than $\frac{\theta_b}{2}$ relative to the elevator in either direction, the drive-train is considered to be in full mesh. Between this region, the elevator is considered unconstrained and its motion is purely a function of aerodynamic forces and the elevator's own internal energy due to inertia. This approach is discussed below.

4.2. Motor State Space Simulation

The motor drive component is treated as a state-space matrix, as given in equation 8.

$$\begin{bmatrix} \dot{\theta} \\ \ddot{\theta} \\ \dot{I} \end{bmatrix} = \begin{bmatrix} 0 & 1 & 0 \\ 0 & -\frac{b}{J} & \frac{K}{J} \\ 0 & -\frac{K}{L} & -\frac{R}{L} \end{bmatrix} \begin{bmatrix} \theta \\ \dot{\theta} \\ I \end{bmatrix} + \begin{bmatrix} 0 \\ 0 \\ \frac{1}{L} \end{bmatrix} V \tag{8}$$

$$y = \begin{bmatrix} 1 & 0 & 0 \end{bmatrix} \begin{bmatrix} \theta \\ \dot{\theta} \\ I \end{bmatrix}$$

where the constants are:

- $b = 4.984 \times 10^{-9}$ N m s is the motor friction constant.
- $J = 1.075 \times 10^{-9}$ kg m^2 is the moment of inertia of the motor armature.
- $K = 777.49 \times^{-6}$ N m A^{-1} is the motor torque constant.
- $R = 15\,\Omega$ is the motor armature resistance.
- $L = 60\,\mu$H is the motor armature inductance.

with computed variables:

- V is the motor applied voltage.
- $I, \dot{I}$ are the motor current and the rate of change of current, respectively.
- $\theta, \dot{\theta}, \ddot{\theta}$ are the motor position, rate, and acceleration, respectively.

The voltage term in equation 8 is computed from a simple PID loop as shown in Figure 3 and derived from [13]. The simulated PID gain terms matched the values used in the physical experiments. The terms $\theta, \dot{\theta}, \ddot{\theta}$ were subsequently divided by the gear ratio of 136, to give the respective position, rate and acceleration of the gearbox output shaft. The gearbox θ_b term was then compared with elevator angle β to discern if the gears were in mesh, or floating in the backlash region.

4.3. Dynamic model of body and elevator

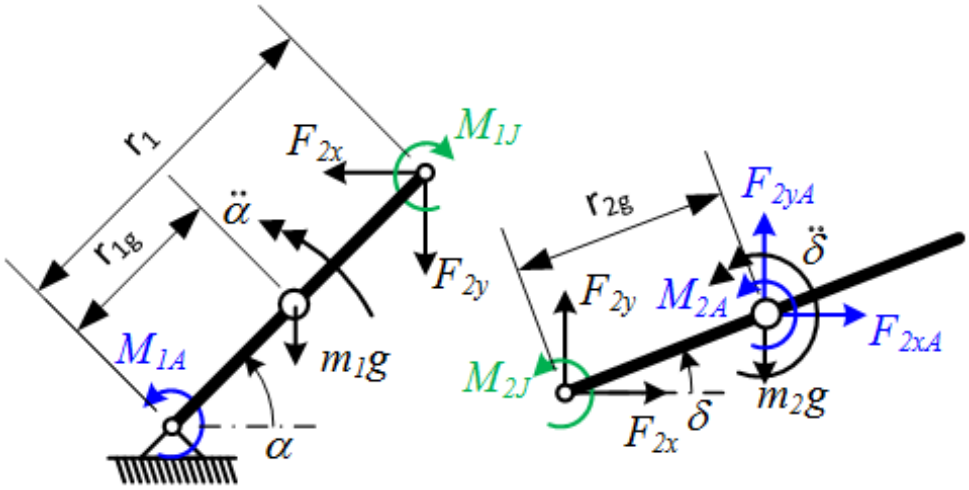

Figure 17. Free-body diagram used for representation of the body and elevator.

The dynamics of the body and elevator are solved by applying D'Alemberts principle [10] to the body and elevator. The resulting free-body diagrams are shown in Figure 17. Resolving moments for the body (link 1) with respect to the pivot yields equation 9 and the elevator (link 2) with respect to its centre of gravity, yields equation 10

$$0 = -I_1\,\ddot{\alpha} + r_1\,\sin(\alpha)\,F_{2x} - r_1\,\cos(\alpha)\,F_{2y} + M_{1A} - M_{1J} - m_1\,r_{1g}\,\cos(\alpha), \quad (9)$$

$$0 = -I_2\,\ddot{\delta} + r_{2g}\,\sin(\delta)\,F_{2x} - r_{2g}\,\cos(\delta)\,F_{2y} + M_{2A} + M_{2J}, \quad (10)$$

where I_1 is the is moment of inertia of the body for rotation about the pivot, I_2 is the moment of inertia of the elevator about its centre of gravity, and M_{1A} and M_{2A} are the aerodynamic moments acting on the two components. In addition, resolving the forces at the centre of gravity of the elevator (link 2) gives

$$0 = -m_2\,\ddot{x} + F_{2x} + F_{2xA}, \quad (11)$$

$$0 = -m_2\,\ddot{y} + F_{2y} + F_{2yA}, \quad (12)$$

where F_{2xA} and F_{2yA} are the aerodynamic forces acting on the elevator. Furthermore, the x and y position of the centre of gravity of the elevator can also be expressed in terms of the body and elevator angles. Differentiating the respective expressions for x and y position allows the accelerations $\ddot{x}$ and $\ddot{y}$ to be expressed in terms of angles, angular velocities, and angular accelerations.

$$\begin{aligned} x &= r_{2g}\,\cos(\delta) + r_1\,\cos(\alpha), \\ \ddot{x} &= -r_{2g}\,\cos(\delta)\,\dot{\delta}^2 - r_{2g}\,\sin(\delta)\,\ddot{\delta} - r_1\,\cos(\alpha)\,\dot{\alpha}^2 - r_1\,\sin(\alpha)\,\ddot{\alpha}, \qquad (13) \\ y &= r_{2g}\,\sin(\delta) + r_1\,\sin(\alpha), \\ \ddot{y} &= -r_{2g}\,\sin(\delta)\,\dot{\delta}^2 + r_{2g}\,\cos(\delta)\,\ddot{\delta} - r_1\,\sin(\alpha)\,\dot{\alpha}^2 + r_1\,\cos(\alpha)\,\ddot{\alpha}. \qquad (14) \end{aligned}$$

Using equations 13 and 14 to eliminate accelerations in equations 11 and 12 and the resulting equations to eliminate the forces at the hinge (F_{2x}, F_{2y}) in equations 9 and 10 yields a set of simultaneous equations of the form

$$\begin{bmatrix} a_{00} & a_{01} \\ a_{10} & a_{11} \end{bmatrix} \begin{pmatrix} \ddot{\alpha} \\ \ddot{\delta} \end{pmatrix} - \begin{pmatrix} c_0' \\ c_1' \end{pmatrix} = \begin{pmatrix} 0 \\ 0 \end{pmatrix}, \qquad (15)$$

with coefficients included in the Appendix 7.

As relative and absolute elevator motion are related by the following relationships

$$\begin{aligned} \beta &= \delta - \alpha, \\ \dot{\beta} &= \dot{\delta} - \dot{\alpha}, \\ \ddot{\beta} &= \ddot{\delta} - \ddot{\alpha}, \end{aligned}$$

we can eliminate $\ddot{\delta}$ from equation 15 to give

$$\begin{bmatrix} a_{00} + a_{01} & a_{01} \\ a_{10} + a_{11} & a_{11} \end{bmatrix} \begin{pmatrix} \ddot{\alpha} \\ \ddot{\beta} \end{pmatrix} - \begin{pmatrix} c_0 - M_{1J} \\ c_1 + M_{2J} \end{pmatrix} = \begin{pmatrix} 0 \\ 0 \end{pmatrix}. \qquad (16)$$

In addition we have split out moment M_{1J} and M_{2J} from c_0' and c_1' as these moments require special consideration based of the state of the gearbox linking the elevator to the motor.

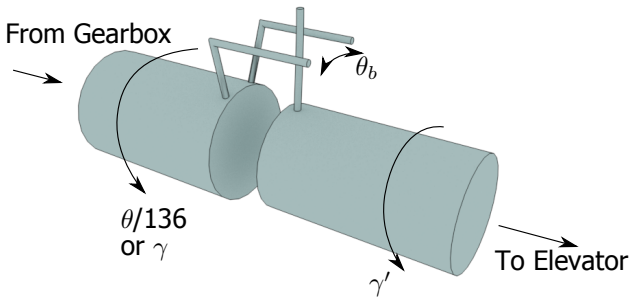

Figure 18. Representation of implemented model to simulate gearbox backlash.

To account for backlash, a model as shown in Figure 18 is employed, which allows the system to operate in three states.

- disconnected (state 0), when two shafts are not engaged ($M_{1J} = M_{2J} = 0$) and the two sides are able to move freely,

- forward engagement (state $+1$), when the gearbox pushes the elevator forwards ($M_{1J} > 0$) , and
- backward engagement (state -1),when the gearbox pushes the elevator backwards ($M_{1J} < 0$).

While the gearbox is engaged (state $= \pm 1$), the moments M_{1J} and M_{2J}, capture two effects. The first term represents the torque generated by the motor, T_{motor}. The second term captures the inertia of the gearbox and motor that needs to rotate as the input shaft rotates in unison with the output shaft. Thus the moments linking body and elevator can be expressed as

$$M_{1J} = T_{motor} G_R, \tag{17}$$
$$M_{2J} = T_{motor}\, G_R - J_0\, G_R^2\, \ddot{\beta}, \tag{18}$$

where G_R is the gearbox ratio.

The dynamic response of the system is calculated by solving equation 16 to obtain the respective accelerations and then using $\ddot{\omega}_{predicted}$ to compute angular velocities and updated angular position using an explicit scheme

$$\dot{\omega}_{predicted} = \dot{\omega}_{old} + \ddot{\omega}_{predicted}\, \Delta t, \tag{19}$$
$$\omega_{predicted} = \omega_{old} + \dot{\omega}_{predicted}\, \Delta t + \frac{1}{2}\, \ddot{\omega}_{predicted}\, \Delta t^2. \tag{20}$$

However, to correctly account for the gearbox state a number of different solution approaches are required to select the correct angular accelerations. For the state 0, positions of the motor output shaft, θ is updated using the state space model given in equation 8 and body and elevator angles are updated by solving equation 16 with $M_{1J} = M_{2J} = 0$. Once the updated positions are available, an engagement check is performed,

$$\text{state} = \begin{cases} -1 & \text{if} \quad G_R\, \beta_{predicted} < \gamma_{predicted} - \frac{1}{2}\, \theta_b \\ 0 & \text{if} \quad \gamma_{predicted} + \frac{1}{2}\, \theta_b \leq G_R\, \beta_{predicted} \leq \gamma_{predicted} - \frac{1}{2}\, \theta_b \\ 1 & \text{if} \quad \gamma_{predicted} - \frac{1}{2}\, \theta_b < G_R\, \beta_{predicted} \end{cases} \tag{21}$$

For the cases that engagement starts, the modelling approximation is that the motion of the elevator will follow the motion of the gearbox. This is a reasonable approximation as the inertia of the elevator, I_2 is significantly less than the apparent inertia of the motor and gearbox, $J_0\, G_R^2$.

Once engagement exists, two parallel evaluations of the predicted elevator angle, β are necessary. The first assumes that gearbox engagement continues and elevator position, β_{load} is predicted by solving equation 16. For this case the motor torque is calculated as

$$T_{motor} = G_R \left(-b\, \dot{\theta}_{old} + K\, I_{old} \right), \tag{22}$$

which is the second row of equation 8 solved for generated torque. Second, a predicted elevator angle, $\beta_{no\,load}$ is evaluated based on the assumption that contact ceases at the start of the time-step, which uses equation 8 to predict shaft angle, $\gamma_{no\,load}$ and equation 16 with $M_{1J} = M_{2J} = 0$ to obtain the angle $\beta_{no\,load}$. By comparing β_{load} and $\beta_{no\,load}$ to $\gamma \pm \frac{1}{2}\theta_b$ it is possible to establish if engagement is maintained of the gearbox disengages. If engagement is maintained, the shaft angle and velocity are set to follow the elevator the first calculation that assumes engagement.

The physical parameters used for the dynamic modelling of the body and elevator motion are summarised in Table 2. These have been normalised to per meter, to match the two-dimensional modelling approach employed by the CFD model.

Furthermore, as there are notable discrepancies between the 2-D and 3-D simulations as identified by TAU and discussed in section 3.2, a scaling factor was applied to compensate for the differences in mean

Table 2. Properties of dynamic model for body and actuator.

Parameter	Value	Parameter	Value
Inertia of body, I_1	7.682×10^{-4} kg m^2 m^{-1}	m_1	598.4×10^{-3} kg m^{-1}
with respect to pivot		r_1	62.5×10^{-3} m
		r_{1g}	50.58×10^{-3} m
Inertia of elevator, I_2	2.818×10^{-6} kg m^2 m^{-1}	m_1	68.6×10^{-3} kg m^{-1}
with respect to CoG		r_2	15×10^{-3} m
		r_{2g}	91.48×10^{-3} m
Inertia of motor, J_0	1.953×10^{-8} kg m^2 m^{-1}	K	7.775×10^{-4} V rad^{-1} s
		L	3.3×10^{-5} H m
		R	0.924 Ω m
		b	9.062×10^{-8} N m rad^{-1} s m^{-1}

pressure and mean moments. These scaling factors proportionally reduce the aerodynamic forces and moments predicted from the 2D CFD before applying them to the dynamic model. The scaling factor for the moment acting on the body, M_{1A} was 0.9 and the scaling factor for the forces acting on the elevator, F_{2xA}, F_{2yA}, M_{2A} was 0.65.

Finally for some cases an initial velocity was prescribed to the body. The requirement to set an initial velocity arises from how the model was supported by a removable support prior to start of the flow, which supported the model trailing edge at -10°AOA. At flow onset, this support is pushed backwards by aerodynamic forces, thereby releasing the model to interact with the flow. However, as the model is sloping downwards, this also results in a vertical upwards motion being applied to the wing and elevator as the support is blown rearwards, resulting in an initial rotation to the elevator. An initial velocity of $\dot{\alpha}$ of 750 rad s^{-1} was selected to ensure the simulation matched the actual data for the first 10 ms after flow onset.

4.4. Results

Closely coupled simulations were performed for both the amplifying and attenuating experiment. In both cases a PID controller controlling the motor voltage, which mimicked the setup used in the experiment was employed. The input signal to the controller are the rotational rate of the body, $\dot{\alpha}$ measured using the Inertial Measurement Unit (IMU) embedded in the body and the position of the elevator, β, measured using a magnetic hall-effect sensor.

The PID controller implemented in the simulations tried to recreate the actual controller shown in Figure 3 as closely as possible, but some modifications were required to accommodate the shorter time-steps of the CFD simulation ($< 1 \times 10^{-7}$ s) compared to the update rate of 8 kHz used by the IMU.

The PID controller operates by setting a target position, $\beta_{command}$ of ± 15 degree, based on the sign of the current body velocity, $\dot{\alpha}$. The following equations show the operation of the controller to set motor voltage, V for the attenuating case.

$$\beta_{command} = \begin{cases} -15° & \text{if} \quad \dot{\alpha} > 0, \\ +15° & \text{if} \quad \dot{\alpha} < 0, \end{cases} \tag{23}$$

$$\begin{aligned} P &= -1\,(\beta - \beta_{command})\,K_P\,C_1; \quad I = 0; \quad D = \dot{\beta}\,K_D\,\frac{1}{8000}\,C_1, \\ V &= (P + I + D)\,V_{max}, \end{aligned} \tag{24}$$

where C_1 is a conversion factor to convert angle to counts used by the micro-controller. For the amplifying case the target position defined in equation 23 is reversed. In both cases controller parameters are $K_P = 5$, $K_I = 0$, and $K_D = 50$. For the current study the integral gain K_I was set to zero to simplify the state machine and as it is expected to have a weak effect on response of

the bang-bang controller. However, wind-up of the integrator term can lead to a brief delay in voltage response, which requires further analysis.

The results for the attenuating simulation are shown in Figure 19. Good agreement exists at the start of the simulation, when both body (α) and elevator (β) closely follow experimental data. Considering Figure 19b, which shows the motor voltage, indicating movement direction of output shaft (θ) and also the two engagement points ($\gamma \pm \frac{\theta_b}{2}$). This shows that the initial upwards motion of the elevator is a direct consequence of the backlash, which allows the elevator to move upwards until it contacts and it is pushed downwards by the motor. After approximately 20 ms the body reaches its first apex, at which point the simulation is seen to overshoot before starting a downwards motion with the correct velocity, but delayed in time. At the same time the elevator is seen to hit its end-stops, which are currently modelled as hard stops, before starting to move upwards. As the body crosses the horizontal (at $t = 40$ ms) a change in slope is seen, however the body continues to overshoot and subsequently fails to recover. At the same time in Figure 19b the elevator is seen to disengage from the gearbox and swing to the other engagement point, a feature that is repeated at $t = 75$ ms. The deviation between the simulation and experiment is most likely caused by the delay in body motion, which results in the elevator providing positive feedback.

Further insight is provided by considering the different moments extracted from the simulation and displayed in Figure 19c. The dominant moments are the moment acting on the body (M_{1A}) and the moment acting on the elevator, resolved back to the pivot location (M'_{2A}). The graph also shows the moments acting at the hinge, M_{2A}, M_{1J}, and T_{motor}. The difference between motor torque and moment transferred to the body arising from the aerodynamic forces and the inertia of the motor and gearbox being accelerated as $\dot{\beta}$ varies.

Figure 20 shows the corresponding results for the amplifying experiment, which used a control system which set the target position, $\beta_{command}$ in the opposite manner to what is shown in equation 23. Here the general trend is recreated more successfully, however predicted motions have a higher frequency, which results in simulations and experimental data running progressively more out of phase. Nevertheless key features from the experimental data are still re-created. The near in-phase motion of the body elevator results in additive moments, which result in the amplification of the oscillatory motion. Especially as time progresses ($t > 40$ ms) it is clear that the motor is caught in the dead-band created by the gearbox backlash and that control input has become minimal.

Considering both simulations and also the comparison between 2D and 3D simulations provided in section 3, several deficiencies of the current simulation approach can be identified, which are also a likely cause for the observed discrepancies. Currently fixed scaling factors are used to correct for 3D effects in this section. However as discussed in section 3.2 this is evidently not correct, and it is anticipated that these would differ for up and down motion as a consequence of the support strut. Furthermore, several of the changes in elevator angle show that the simulated motor accelerates at a higher rate, which is most likely due to the current state space model not capturing certain frictional losses and sticktion. Future work will seek to perform closely coupled 3-D simulations and use better characterised hardware (e.g. better friction models), which will reduce or eliminate the major modelling assumptions in the current work.

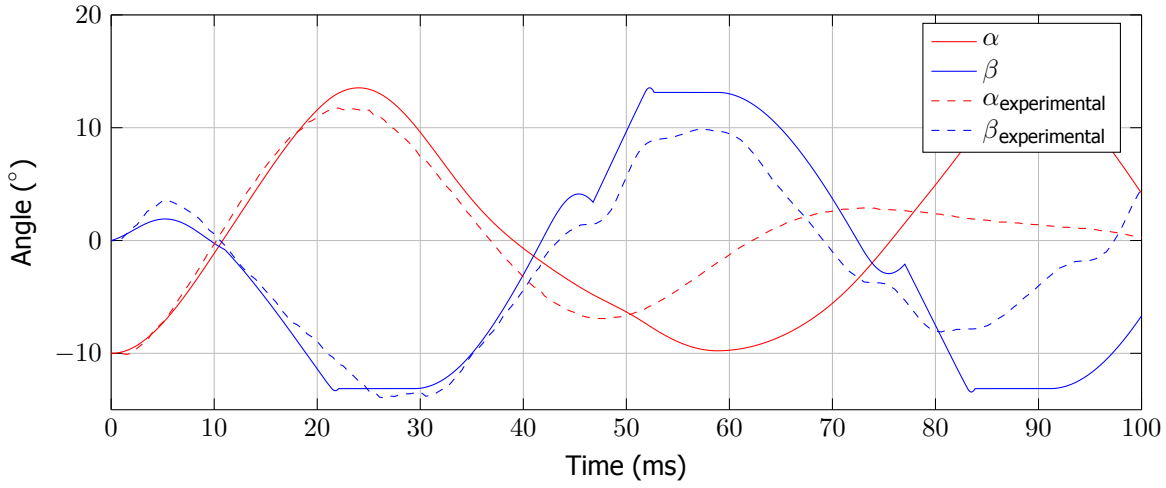

(a) Angular position of body, α and elevator, β.

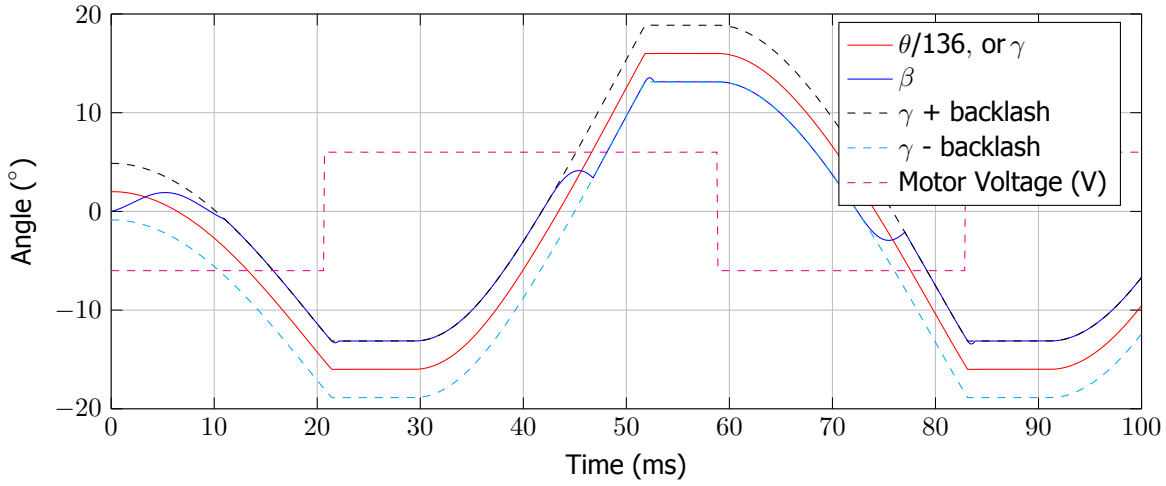

(b) Angular position of elevator, β together with the backlash limits imposed by the gearbox shaft, $\gamma \pm \frac{1}{2}\theta_b$, and motor Voltage.

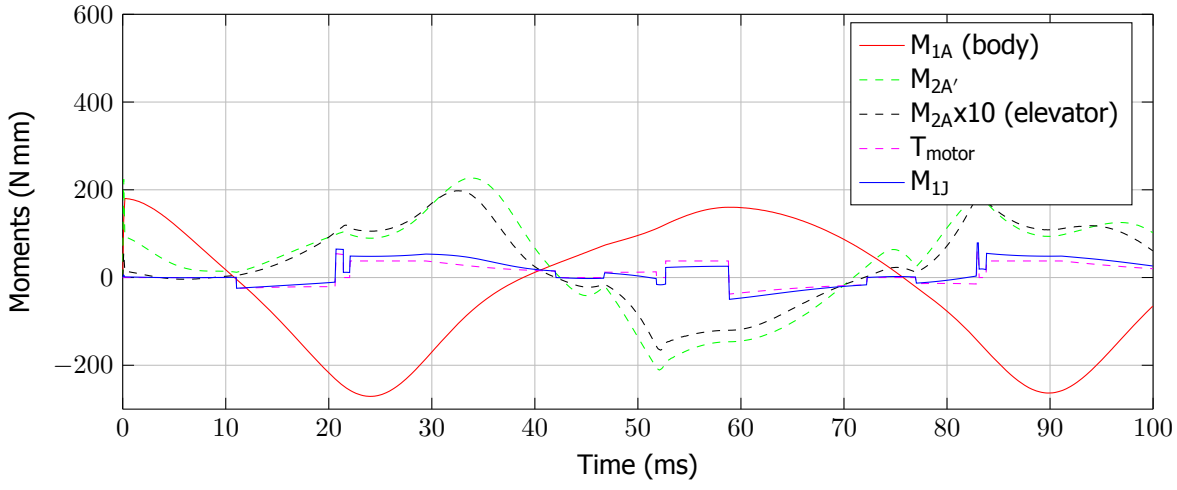

(c) Aerodynamic and hinge moment acting on the body and elevator.

Figure 19. Results from closely coupled CFD simulation examining the attenuating case.

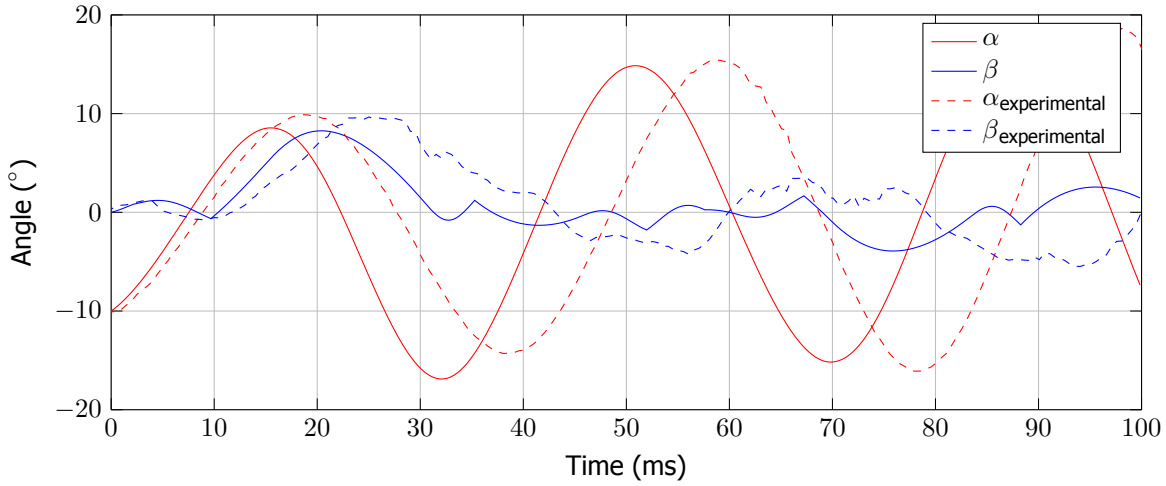

(a) Angular position of body, α and elevator, β.

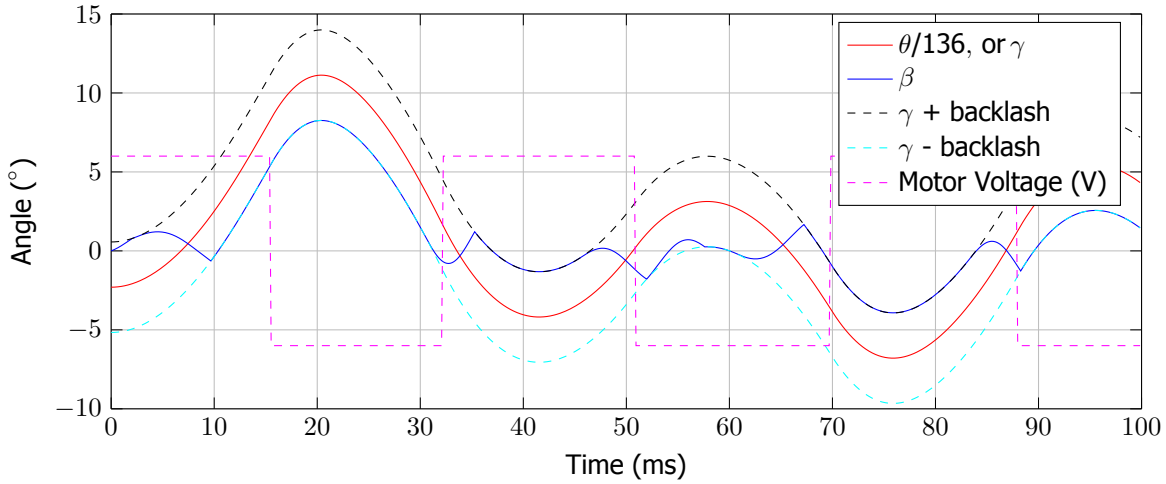

(b) Angular position of elevator, β together with the backlash limits imposed by the gearbox shaft, $\gamma \pm \frac{1}{2}\theta_b$, and motor Voltage.

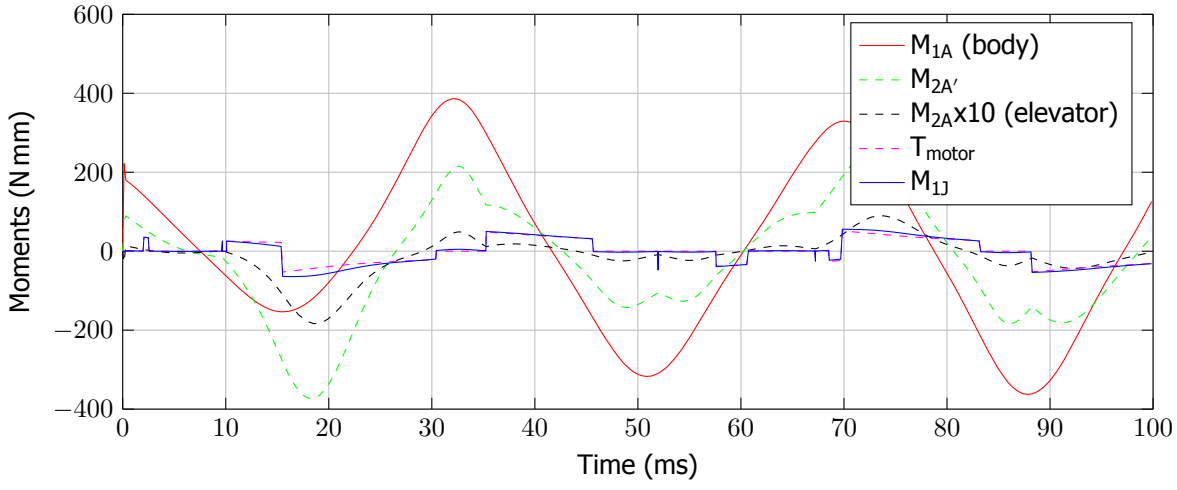

(c) Aerodynamic and hinge moment acting on the body and elevator.

Figure 20. Results from closely coupled CFD simulation examining the amplifying case.

5. Conclusions

Models with dynamically actuated surfaces have been used in the TUSQ facility to attempt to demonstrate that ground-test facilities can be used for developing control approaches which can be applied to real-world vehicles.

Simulation with 2D and 3D software were completed and they showed good correlation with experimental results. Using 2D simulations, to reduce computational time, a dynamically controlled state-machine of the system was developed, and shown to capture the motor, gearbox, and backlash behaviour.

This paper however explains the need to use caution when interpreting the results; whilst 2D simulation reduced processing time, the 2D simulations don't incorporate the actual 3D flow effects such as spillage over the side of the model, non-uniform pressure distributions in a span-wise direction, or the additional interactions with the model support structure. These 3D effects can cause large variations in calculated moments, with 2D simulations over-estimating the aerodynamic moments by up to a factor of 4.5. These variations were covered in the 2D simulation including non-linear scaling effects.

Research into control simulations by using steady state 3D results from TAU as a lookup table for dynamic simulations is ongoing, as is development of new physical models, to address the pressure transducer clipping and non-linear effects of backlash in the elevator drive-train.

6. Acknowledgements

Nathan Stern is supported by an Australian Government Research Training (RTP) Scholarship.
This research was supported by AFOSR under Grant FA2386-16-1-4024.
Rishabh Choudhury is sponsored by the European Space Agency (ESA) International Research Fellowship as part of the international collaboration framework between ESA and Australia.

7. Appendix

Definition of coefficients used in Equation 16.

$$
\begin{aligned}
a_{00} &= -I_1 + m_2\, r_1^2\, (-\sin(\alpha)\, \sin(\alpha) - \cos(\alpha)\, \cos(\alpha)) \\
a_{01} &= m_2\, r_1\, r_{2g}\, (-\sin(\alpha)\, \sin(\delta) - \cos(\alpha)\, \cos(\delta)) \\
a_{10} &= m_2\, r_1\, r_{2g}\, (-\sin(\delta)\, \sin(\alpha) - \cos(\delta)\, \cos(\alpha)) \\
a_{11} &= -I_2 + m_2\, r_{2g}\, (-\sin(\delta)\, \sin(\delta) - \cos(\delta)\, \cos(\delta)) \\
c_0 &= M_{1A} - m_1\, g\, r_{1g}\, \cos(\alpha) \\
&\quad + r_1\, m_2\, \sin(\alpha)\, (-r_{2g}\, \cos(\delta) \dot{\delta}^2 - r_1\, \cos(\alpha) \dot{\alpha}^2) \\
&\quad - r_1\, m_2\, \cos(\alpha)\, (-r_{2g}\, \sin(\delta) \dot{\delta}^2 - r_1\, \sin(\alpha)\, \dot{\alpha}^2) \\
&\quad - r_1\, \sin(\alpha)\, F_{x2A} + r_1\, \cos(\alpha)\, F_{y2A} - r_1\, \cos(\alpha)\, m_2\, g \\
c_1 &= M_{2A} \\
&\quad + r_{2g}\, m_2\, \sin(\delta)\, (-r_{2g}\, \cos(\delta)\, \dot{\delta}^2 - r_1\, \cos(\alpha)\, \dot{\alpha}^2) \\
&\quad - r_{2g}\, m_2\, \cos(\delta)\, (-r_{2g}\, \sin(\delta) \dot{\delta}^2 - r_1\, \sin(\alpha) \dot{\alpha}^2) \\
&\quad - r_{2g}\, \sin(\delta)\, F_{x2A} + r_{2g}\, \cos(\delta)\, F_{y2A} - r_{2g}\, \cos(\delta)\, m_2\, g \\
c_0' &= c_0 - M_{1J} \\
c_1' &= c_1 + M_{2J}
\end{aligned}
$$

References

[1] Byrenn Birch, David Buttsworth, Rishabh Choudhury, and Nathan Stern. Characterization Of A Ludwieg Tube With Free Piston Compression Heating In Mach 6 Configuration. In *22nd AIAA International Space Planes and Hypersonics Systems and Technologies Conference*, 2018.

[2] David R Buttsworth, Nathan Stern, and Rishabh Choudhury. A Demonstration of Hypersonic Pitching Control in the TUSQ Hypersonic Wind Tunnel. In *55th AIAA Aerospace Sciences Meeting*, 2017.

[3] R. J. Gollan and P. A. Jacobs. About the formulation, verification and validation of the hypersonic flow solver Eilmer. *International Journal for Numerical Methods in Fluids*, 73(1), 2013.

[4] Peter Jacobs and Rowan Gollan. Implementation of a Compressible-Flow Simulation Code in the D Programming Language. In *Advances of Computational Mechanics in Australia*, volume 846 of *Applied Mechanics and Materials*. Trans Tech Publications, 9 2016. doi: 10.4028/www.scientific.net/AMM.846.54.

[5] Institute of Aeronautics and German Aerospace Centre (DLR) Flow Technology. The DLR TAU code, 2012. URL `http://tau.dlr.de/`.

[6] Patrick H Oosthuizen and William E Carscallen. *Compressible fluid flow*. McGraw-Hill, 1997.

[7] P Petrie-Repar. Numerical simulation of diaphragm rupture. Phd thesis, University of Queensland, Mechanical Engineering, 1997.

[8] D. I. Pullin. Direct simulation methods for compressible inviscid ideal-gas flow. *Journal of Computational Physics*, 34(2), 1980.

[9] K. Qin, I.H.J. Jahn, R. Gollan, and P. Jacobs. Development of a Computational Tool to Simulate Foil Bearings for Supercritical CO2 Cycles. *Journal of Engineering for Gas Turbines and Power*, 138(9), 2016.

[10] G.H Ryder and M.D Bennett. *Mechanics of Machines*. Macmillan Press Ltd., 1994.

[11] Nathan Stern, David Buttsworth, Byrenn Birch, and Rishabh Choudhury. Hypersonic Pitching Control Model Development. In *22nd AIAA International Space Planes and Hypersonics Systems and Technologies Conference*, 2018.

[12] Y. Wada and M. S. Liou. A flux splitting scheme with high-resolution and robustness for discontinuities. AIAA Paper 94-0083, January 1994.

[13] Tim Wescott. *Applied Control Theory for Embedded Systems (Embedded Technology)*. Newnes, Newton, MA, USA, 2006. ISBN 0750678399.